

# Strong Storm-effect behaviors of topside and bottom-side ionosphere under low solar activity: Case study in the geomagnetic storm during 25-27 August 2018

Wang Li<sup>1</sup>, Dongsheng Zhao<sup>2</sup>, Changyong He<sup>3</sup>, Yi Shen<sup>4</sup>, Craig M Hancock<sup>5</sup>, and Kefei Zhang<sup>2</sup>

<sup>1</sup>Kunming University of Science and Technology

<sup>2</sup>China University of Mining and Technology

<sup>3</sup>Hunan University of Science and Technology

<sup>4</sup>Xinyang Normal University

<sup>5</sup>School of Architecture, Building and Civil Engineering, Loughborough University

November 24, 2022

## Abstract

The 25-27 August geomagnetic storm was the third largest storm in 24th solar cycle, which was a surprising space event that generated in the background of very low solar activity. This study presents an overview of temporal-spatial behaviors of ionospheric plasma irregularities as functions of geographic longitude, latitude and altitude by ground-based (GNSS receivers and ionosonde) instruments and space-borne (Swarm-A and Swarm-B) satellites. The results not only reveal the enhanced equatorial ionization anomaly (EIA) and hemispheric asymmetry over the Asian-Australian and American sectors in a particular time, but also discover the development of hemispheric asymmetric features of global ROTI in the main and recovery phases. In addition, this storm also triggered positive plasma irregularities in altitudes of 100 to 150km near Auroral zone, and the changed ratio of bottom-side plasma irregularities exceeded 250%, which has been cross validated by multiple instrument and TIE-GCM's simulation. Furthermore, the thermospheric density ratio  $O/N_2$ , equatorial electrojet and vertical  $E \times B$  drifts suffered from the storm largely, the equatorial and mid-latitude plasma irregularities may be a combined action of thermospheric composition change, equatorial electrojet and vertical  $E \times B$  drifts. Finally, the storm also induced positive Joule heating irregularities in Auroral ionosphere in altitudes of 100 to 400km with a maximum changed ratio of  $>200\%$ , as well as the cross Polar voltage enhanced to  $\sim 90$ kv. The Polar ionospheric irregularities may be associated with the additional energy input through the ways of particle precipitation, Joule heating and ionospheric currents intensification.

1 **Strong Storm-effect behaviors of topside and bottom-side ionosphere under**  
2 **low solar activity: Case study in the geomagnetic storm during 25-27**  
3 **August 2018**

4 **Wang Li<sup>1,2</sup>, Dongsheng Zhao<sup>2\*</sup>, Changyong He<sup>3</sup>, Shen Yi<sup>4</sup>, Craig M. Hancock<sup>5</sup>, Kefei**  
5 **Zhang<sup>2</sup>**

6 <sup>1</sup> Faculty of land resources engineering, Kunming University of Science and Technology,  
7 Kunming, China.

8 <sup>2</sup> School of Environmental Science and Spatial Informatics, China University of Mining and  
9 Technology, Xuzhou, China.

10 <sup>3</sup> National-Local Joint Engineering Laboratory of Geo-Spatial Information Technology,  
11 Hunan University of Science and Technology, Xiangtan, China.

12 <sup>4</sup> Key Laboratory for Synergistic Prevention of Water and Soil Environmental Pollution,  
13 Xinyang Normal University, Xinyang, China.

14 <sup>5</sup> School of Architecture, Building and Civil Engineering, Loughborough University,  
15 Loughborough, United Kingdom.

16 Corresponding author: Dongsheng Zhao ([dszhao\\_gnss@foxmail.com](mailto:dszhao_gnss@foxmail.com))

17  
18 **Key points:**

- 19 ● First time to give an overview of the development of global Rate of total electron content  
20 (TEC) Index change in the whole phase of storm
- 21 ● Positive ionospheric plasma irregularities in the altitudes of 100 to 150km were only  
22 detected near Auroral zone ( $> \sim 50^\circ\text{N/S}$ )
- 23 ● Low-middle latitude plasma irregularities were a combined action of density ratio  $O/N_2$ ,  
24 equatorial electrojet and vertical  $E \times B$  drift

## 28 **Abstract**

29       The 25-27 August geomagnetic storm was the third largest storm in 24th solar cycle, which  
30 was a surprising space event that generated in the background of very low solar activity. This  
31 study presents an overview of temporal-spatial behaviors of ionospheric plasma irregularities  
32 as functions of geographic longitude, latitude and altitude by ground-based (GNSS receivers  
33 and ionosonde) instruments and space-borne (Swarm-A and Swarm-B) satellites. The results  
34 not only reveal the enhanced equatorial ionization anomaly (EIA) and hemispheric asymmetry  
35 over the Asian-Australian and American sectors in a particular time, but also discover the  
36 development of hemispheric asymmetric features of global ROTI in the main and recovery  
37 phases. In addition, this storm also triggered positive plasma irregularities in altitudes of 100  
38 to 150km near Auroral zone, and the changed ratio of bottom-side plasma irregularities  
39 exceeded 250%, which has been cross validated by multiple instrument and TIE-GCM's  
40 simulation. Furthermore, the thermospheric density ratio  $O/N_2$ , equatorial electrojet and  
41 vertical  $E \times B$  drifts suffered from the storm largely, the equatorial and mid-latitude plasma  
42 irregularities may be a combined action of thermospheric composition change, equatorial  
43 electrojet and vertical  $E \times B$  drifts. Finally, the storm also induced positive Joule heating  
44 irregularities in Auroral ionosphere in altitudes of 100 to 400km with a maximum changed ratio  
45 of  $>200\%$ , as well as the cross Polar voltage enhanced to  $\sim 90$ kv. The Polar ionospheric  
46 irregularities may be associated with the additional energy input through the ways of particle  
47 precipitation, Joule heating and ionospheric currents intensification.

48 **Key words:** ionospheric disturbances, geomagnetic storm, hemispheric asymmetry, TIE-GCM,  
49  $O/N_2$

50 **Plain language:** Large amounts of charged particles deposited in the thermosphere-ionosphere  
51 system during a strong geomagnetic storm, this process could change global ionospheric  
52 convection and weaken the activities of positioning, navigation, radio communication, etc. This  
53 study tries to discover the spatial-temporal changes of global ionosphere under the strong  
54 geomagnetic storm during 25-27, August 2018. From the observations of Global Navigation  
55 Satellite System (GNSS) receivers and radars, we first time to discover the spatial-temporal  
56 evolutions of global plasma irregularities, and reveal the storm-enhanced equatorial ionization

57 anomaly and hemispheric asymmetry in the Asian-Australian and American sectors. Besides,  
58 positive plasma irregularities in the altitudes of 100 to 150km were only near Auroral zone (>  
59  $\sim 50^\circ\text{N/S}$ ), rather than in low-middle latitudes. Furthermore, the potential drivers are  
60 investigated for explaining the plasma irregularities. The equatorial and mid-latitude  
61 irregularities may be a combined action of thermospheric composition change, equatorial  
62 electrojet and vertical  $E \times B$  drifts. The Polar ionospheric irregularities may be associated with  
63 the additional energy input through the ways of particle precipitation, Joule heating and  
64 ionospheric currents intensification.

## 65 **1. Introduction**

66 Ionosphere has a serious effect on absorbing, scattering and refracting radio signals, which  
67 is a main error source in the navigation and positioning service. Now the global navigation  
68 satellite system (GNSS) differential technique and empirical/theoretical models are usually  
69 used to correct the ionospheric delay. However, ionospheric plasma during severe geomagnetic  
70 storms suddenly increases or decreases violently, which easily reduces the accuracy of  
71 positioning and navigation. Now available techniques are not good at correcting severe storm-  
72 effect ionospheric perturbations; therefore, it is necessary and valuable to investigate the  
73 ionospheric spatial-temporal behaviors response to strong magnetic storms and to discuss the  
74 probable drivers.

75 Geomagnetic storm usually has a severe effect on the ionospheric system, auroral particle  
76 precipitation, Polar ionospheric currents and convection are reinforced largely during a  
77 geomagnetic storm. The enhanced Polar ionospheric ionization and electric fields penetrate to  
78 low-middle latitudes, this process affects global electrodynamics and changes the structure of  
79 the thermospheric-ionospheric system remarkably. The Joule heating and Auroral particle  
80 precipitation heat and expand the thermosphere, which further changes the composition and  
81 dynamics of the thermospheric-ionospheric system [Astafyeva *et al.*, 2015]. With rapid  
82 development of Global Navigation Satellite System (GNSS) and radio occultation, the storm-  
83 effect ionospheric behaviors have been paid more attention by multiple ground-based and  
84 space-borne techniques. The “Halloween” storm erupted on 29-30, October 2003 was one of  
85 strongest geomagnetic storms in this century. After a few hours when the interplanetary

86 magnetic field suddenly turned southward, the dayside ionospheric total electron content (TEC)  
87 increased about 40%, and the Challenging Minisatellite Payload (CHAMP) profiles indicated  
88 the dayside TECs over mid-latitudes increased ~900% on 30 October [Mannucci et al., 2005].  
89 The significant increments of TEC and peak density (NmF2) were also observed over the  
90 European and North African sectors during a following stronger geomagnetic storm occurred  
91 on November 20, 2003 [Crowley et al., 2006]. Moreover, the sudden ionospheric irregular  
92 behaviors response to geomagnetic storms were also been reported over Jicamarca [Zhang et  
93 al., 2019], Brazilian equatorial–low latitudes [de Paula et al., 2019], China and adjacent areas  
94 [Aa et al., 2018], Asian-Australian sector [Lei et al., 2018], Indian sector [Ramsingh et al.,  
95 2015], Turkey [Karataş, 2020], Arctic and Antarctic [Durgonics et al., 2017; Mitchell et al.,  
96 2005; Shreedevi et al., 2020] and in a global scale [Atıcı and Sağır, 2020; Li et al., 2022]. These  
97 reports revealed that strong geomagnetic storms easily triggered large-scale positive or  
98 negative traveling ionospheric disturbances (TIDs), and sometimes the TIDs had a significant  
99 latitudinal asymmetric structure in northern-southern hemispheres that is caused by the  
100 displaced magnetic poles and seasonal asymmetries in the thermosphere-ionosphere system.  
101 Multi-instruments observations and theoretical model simulations were conducted for  
102 explaining the disturbed ionospheric dynamic convections, and the results concluded that the  
103 negative TIDs were primarily attributed to a decrement of the thermospheric density ratio O/N<sub>2</sub>  
104 [Dmitriev et al., 2017; Fuller - Rowell et al., 1994]. However, the drivers for positive TIDs  
105 were various, thermospheric neutral winds, disturbance dynamo electric fields (DDEF), prompt  
106 penetration electric field (PPEF) as well as charged particle precipitation, had been reported to  
107 be the potential factors in enhancing plasma densities [Atıcı and Sağır, 2020; Crowley et al.,  
108 2006; Nava et al., 2016; Qian et al., 2019; Richmond and Lu, 2000].

109 Ionospheric storms primarily occur as a consequence of strong coronal mass ejection  
110 (CME), such as the magnetic storms in 22-23, June 2015 [Ngwira et al., 2019] and 7-8,  
111 September 2017 [Li et al., 2018a]. However, the 25-27, August 2018 space event that is the  
112 third largest magnetic storm in 24<sup>th</sup> solar cycle happened after a slowly moving CME on 20  
113 August, it is a huge surprise that the weak CME that even didn't show a sudden impulse could  
114 trigger a strong ionosphere-thermosphere response. The positive and negative ionospheric  
115 perturbations over North America [Cherniak and Zakharenkova, 2022], Brazil [Spogli et al.,

116 2021], Asia [Lissa *et al.*, 2020], Middle latitudes [Chang *et al.*, 2022], as well as the global  
117 [Astafyeva *et al.*, 2020] response to the surprising space event have been reported. This  
118 geomagnetic storm induced penetration electric fields created favorable conditions for strong  
119 fountain effect enhanced equatorial ionization anomaly (EIA) and generated equatorial plasma  
120 bubbles (EPBs). The EPBs appeared over a larger latitudinal extent of EIA crests, while the  
121 plasma density in the western coast of North America depleted in the northwestward direction  
122 [Cherniak and Zakharenkova, 2022]. The Defense Meteorological Satellite Program (DMSP)  
123 also detected midlatitude plasma depletion in the Asian sector, the local TIDs were responsible  
124 for the midlatitude plasma depletion in Asia and United States, rather than the absence of EPBs  
125 [Chang *et al.*, 2022]. Different from the mid-latitude plasma depletion in the northern  
126 hemisphere, Spogli *et al.* [2021] used the situ measurements provided by China Seismo-  
127 Electromagnetic Satellite and by Swarm-A satellite with ground-based observations to reveal  
128 the ionospheric response at low-middle latitudes over Brazil, and found that significant foF2  
129 increments appeared over the ionosondes located at both of dip-equator and southern crest of  
130 the EIA. The decrease of the eastward electric field was the main driver for the equator station,  
131 while it was resulted from the storm-induced equatorward thermospheric winds for the crest  
132 station. In addition, unprecedented hemispheric asymmetries of the thermospheric-ionospheric  
133 responses were also observed during the main and recovery phases of the storm, which  
134 expressed that strong positive plasma storms occurred in the northern hemisphere at the  
135 beginning of the space event, while an extreme expansion of the thermospheric composition  
136 ratio O/N<sub>2</sub> appeared in the opposite hemisphere during the recovery phase. The seasonal  
137 asymmetry in the high-latitude plasma and neutral mass density distributions along with the  
138 asymmetries in the geomagnetic field played a decisive role for the hemispheric asymmetric  
139 structure of disturbed plasma [Astafyeva *et al.*, 2020].

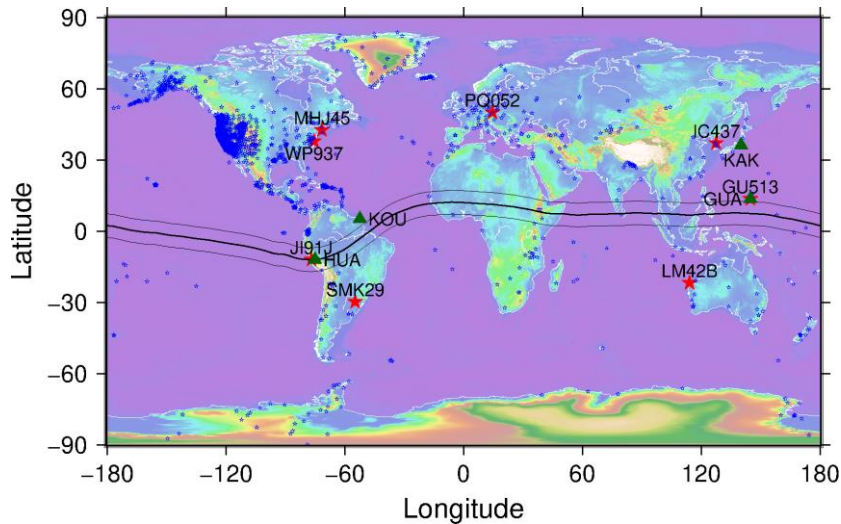
140 Most of previous studies focused on the planar ionospheric response (TEC) to the storm,  
141 but the altitudinal plasma behavior was still not clear. Besides, the storm-effect ionospheric  
142 response is controlled by multiple drivers at a particular moment of time and in particular  
143 location. The present study has the objectives to examine: (1) the development of hemispheric  
144 asymmetry of plasma irregularities in the main and recovery phase; (2) the altitudinal behaviors  
145 of plasma irregularities in low-middle latitudes and auroral zone; (3) the potential drivers for

146 the latitudinal plasma irregularities over the Asian-Australian and American sectors. To address  
147 these objectives, the latitudinal ionospheric irregularities are detected by a set of ground-based  
148 (GNSS receiver and digital-ionosonde) and space-borne (SWARM) instruments, and the  
149 potential drivers for the equatorial-auroral irregularities are discussed by a set of magnetometer,  
150 SuperDARN, Global Ultraviolet Imager (GUVI) and TIE-GCM's simulation.

## 151 **2. Datasets**

152 In order to analyze planar-vertical behaviors of global plasma irregularities during the  
153 magnetic storm on 25-27, August 2018 completely, the ground-based (GNSS receiver and  
154 ionosonde) observations and the plasma profiles derived from the space-borne Swarm  
155 constellation are used. In addition, the horizontal components of the magnetic field,  
156 thermospheric density ratio  $O/N_2$  and the TIE-GCM's simulations are also adopted for  
157 explaining the drivers of plasma irregularities. The geographic locations of ground-based  
158 instruments are shown in Figure 1, and more detail information of several kinds of datasets are  
159 introduced as follows.

160 The GNSS observations are obtained from the University NAVSTAR Consortium  
161 (UNAVCO) that provides access to geodetic GPS/GNSS data used for geoscience research and  
162 education. The UNAVCO provides about 2500 Receiver Independent Exchange Format  
163 (RINEX) files daily through the link <https://www.unavco.org/data/gps-gnss/gps-gnss.html>. It  
164 should be noted that the vertical total electron content (VTEC) estimated by the carrier-phase  
165 smoothed pseudo-range method is used to investigate the ionospheric perturbations during the  
166 geomagnetic storm [Li *et al.*, 2018b]. For similarity, the TEC signifies VTEC in the whole  
167 study. In addition, two chain digital-ionosondes located at the Asian-Australian and American  
168 sectors are also utilized to investigate the vertical behaviors of storm-induced plasma  
169 irregularities. Due to the influence of geomagnetic storm, the digital-ionosonde in the Asian  
170 sector fails to observe the auroral plasma irregularities. The ionosonde PQ052 (14.6°E, 50°N)  
171 located at Pruhonice in Europe is selected. The sounder profiles of two chains can be obtained  
172 from the Lowell DIDBase (`jdbc:firebirdsql://didbase.giro.uml.edu/didb`) via the SAO explorer.



173

174 **Figure 1.** Spatial distribution of GNSS stations, ionosondes and magnetometers. The blue pentagrams  
 175 signify global GNSS stations, the red pentagrams signify the ionosondes located at the Asian-Australian  
 176 and American sectors, the green triangles signify magnetometers, and the solid and dashed curves depict  
 177 the location of the magnetic equator and the region of equatorial electrojet.

178 Swarm consists of three microsattellites (Alpha, Bravo and Charlie) that are placed in two  
 179 different orbital planes, among them the Swarm-A and Swarm-C fly at a mean altitude of  
 180 450km, and the satellite Swarm-B places in a mean altitude of 530km. In this study, the electron  
 181 density profiles of Swarm-A and Swarm-B are selected to analyze the plasma irregularities,  
 182 and the electron density is derived from the high gain ion current that is determined by the  
 183 Langmuir probe. The Swarm profiles can be obtained from the website  
 184 [https://swarmdiss.eo.esa.int/#swarm%2FLevel2daily%2FEntire\\_mission\\_data%2FTEC%2FTMS](https://swarmdiss.eo.esa.int/#swarm%2FLevel2daily%2FEntire_mission_data%2FTEC%2FTMS).  
 185 In addition, the daily F10.7 index, 81-day mean F10.7 and Kp index are imported to the  
 186 TIE-GCM model as input parameters, and the output parameters include electron density,  
 187 neutral winds, thermospheric composition and electric field. More details about the TIE-GCM,  
 188 the readers please refer to <https://www.hao.ucar.edu/modeling/tgcm/tie.php>. For improving the  
 189 simulated accuracy of the TIE-GCM products response to geomagnetic storms, the period of  
 190 the TIE-GCM products is from 00:00 (Universal Time, UT), 23 August to 29 August 2018.

### 191 **3. Results**

#### 192 **3.1 Solar-terrestrial environment**

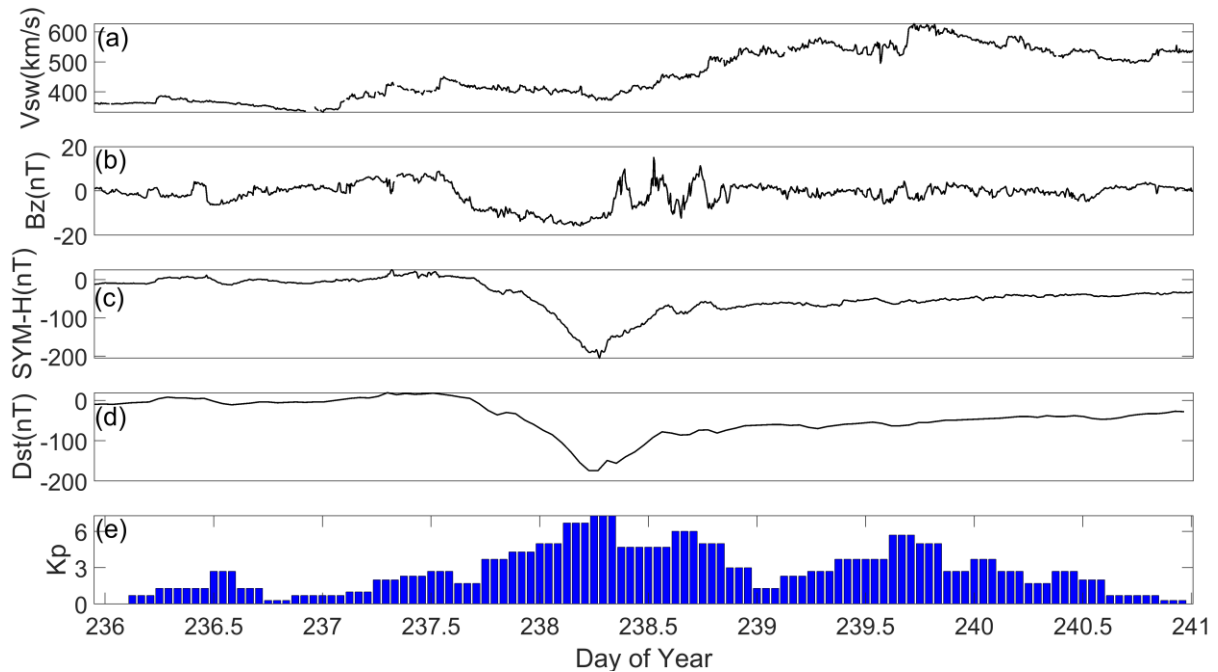
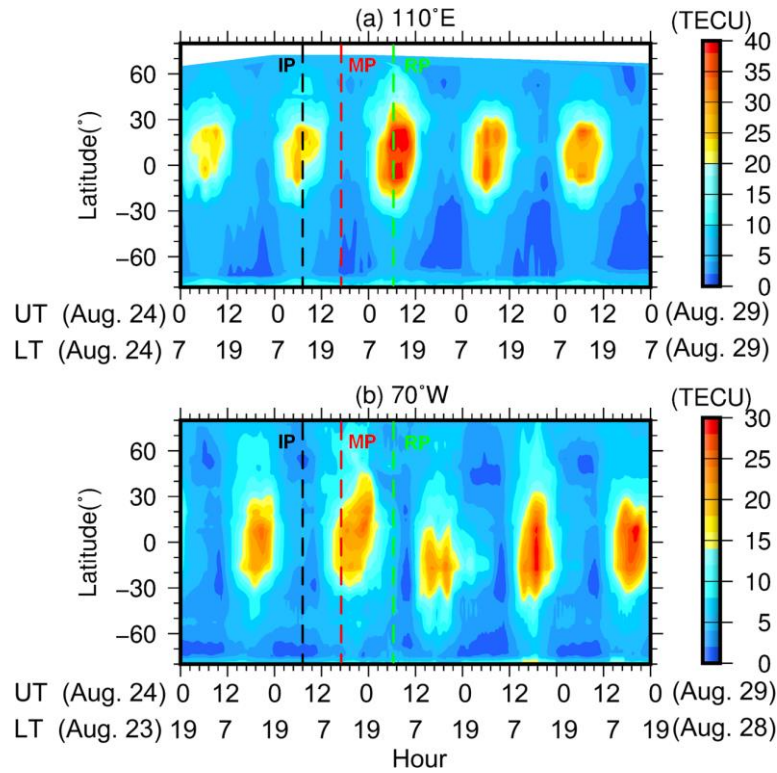


**Figure 2.** Variations of solar-terrestrial indices during day of year (DOY) 236 to 240 in 2018

Solar-geomagnetic change is an important factor in effecting the process of ionospheric plasma irregularities during storms. Therefore, the data of solar wind speed ( $V_{sw}$ ), interplanetary magnetic field, and geomagnetic indices obtained from the Goddard Space Flight Center (<https://omniweb.gsfc.nasa.gov/form/dx1.html>) is analyzed. The record third largest geomagnetic storm in the 24<sup>th</sup> cycle was initiated from a slow CME on 20 August 2018, which arrived at the earth thermosphere-ionosphere system on 25 August. As shown in Figure 2, the solar-terrestrial indices were in a quiet level before UT14, DOY 237 (25 August), and a strong geomagnetic storm happened from UT14, DOY237 to DOY 239 (27 August). Figure 2(a) shows the  $V_{sw}$  was low with a mean velocity of 400 to 450km/s in the main phase (UT14, DOY237 - UT7, DOY238) of the geomagnetic storm, while it enhanced abruptly in the recovery phase with a maximum speed of 620km/s. Figure 2(b) shows the  $B_z$  component of interplanetary magnetic field (IMF) had an abrupt southward excursion. From UT14, DOY237, the  $B_z$  turned southward with a minimum value of -18nT in the forenoon of DOY 238. The horizontal component of longitudinally symmetric disturbances (SYM-H) is essentially the same as the Dst index to describe the mid-latitude geomagnetic disturbances. Figure 2(c) and 2(d) express that both SYM-H and Dst had a significant negative excursion since the afternoon of DOY 237, and these indices reached to minimum values of  $\sim$ -200nT and  $\sim$ -180nT at UT06-

212 08, DOY 238, respectively. As well as the global geomagnetic field indexed by Kp enhanced  
 213 to a maximum level of 7. According to the classification of geomagnetic storm released by  
 214 National Oceanic and Atmospheric Administration (NOAA), this storm is classed as “strong”.

215 **3.2 Ionospheric irregularities over the Asian-Australian and American sectors**

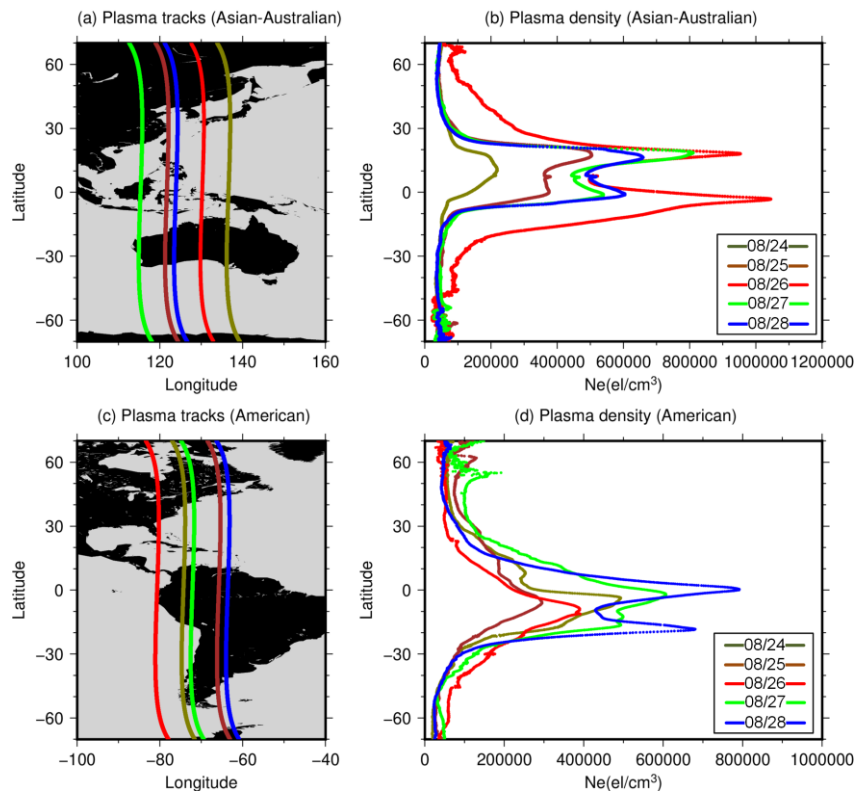


216  
 217 **Figure 3.** Latitudinal TEC changes along (a) 110°E, (b) 70°W longitudes during August 24-28, the dashed  
 218 black line signify the initial phase (IP) of the geomagnetic storm, the dashed red line signify the main  
 219 phase (MP), and the dashed green line signify the recovery phase (RP). White color depicts empty cells  
 220 due to lack of actual observations.

221 The dual-frequency observations of about 2500 GNSS receivers provided by UNAVCO  
 222 are used to estimate the global TEC map, then the TEC grid maps are constructed by Kriging  
 223 interpolation method. The north-south cross-sections (keograms) of the GNSS TEC maps along  
 224 the 110°E and 70°W longitudes during 24-28 August are plotted to illustrate the temporal  
 225 evolution of the storm-effect TEC changes over two sectors. These keograms, plotted as a  
 226 function of UT time and geographic latitude, as shown in Figure 3. Figure 3(a) demonstrates  
 227 that in the Asian-Australian sector, the ionospheric TEC kept in a low level of 20 to 25TECU.  
 228 In the main phase of the storm, the equatorial ionospheric TEC enhanced significantly with a

229 double peak structure that coincided to the Dst index decreased to a maximum value of -174nT.  
 230 The enhanced TEC primary occurred in the ending of main phase and the beginning of recovery  
 231 phase (UT04-10, 26 August), the maximum TEC reached to 40TECU.

232 Different from the TEC change over the Asian-Australian sector, Figure 3(b) found a  
 233 significant hemispheric asymmetric structure of TEC irregularity in the American sector. For  
 234 example, significant TEC depletion happened over the American sector in the recovery phase.  
 235 In the afternoon of 26 August, the TEC in the northern hemisphere depleted from 15-20TECU  
 236 to 10TECU, while the equatorial and mid-latitude TEC in the opposite hemisphere enhanced  
 237 about 5TECU. The positive TEC storm was stronger in the afternoon of following two days,  
 238 and the maximum enhanced TEC exceeded 30TECU. Figure 3 concludes that the geomagnetic  
 239 storm triggered an asymmetric ionospheric storm, and the occurred phases of ionospheric storm  
 240 over different longitudes had a particular diversity.

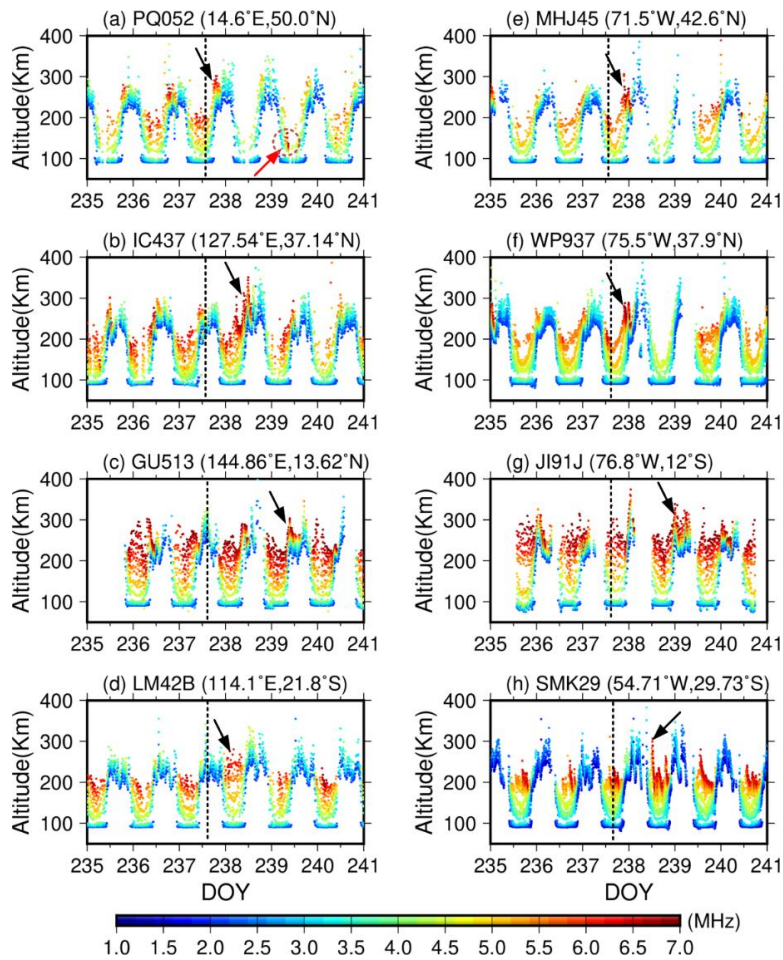


241 **Figure 4.** Daily changes of Ionospheric electron density detected by Langmuir probe instrument onboard  
 242 Swarm-A satellite during (a-b) the main phase over the Asian-Australian sector (c-d) and the recovery  
 243 phase over the American phase from 24 to 28 August.  
 244

245 Figure 4 gives an overview on the daily development of storm-effect ionospheric electron  
 246 density ( $N_e$ ) as measured by the space-borne Swarm-A satellite that flies at an orbital altitude

247 of  $\sim 450$  km. Here, the electron density signifies the amounts of plasma at the Orbital altitude of  
248 Swarm-A, which is useful to reveal the change of topside ionosphere during the storm. The  
249 result in Figure 3 demonstrates that the storm-induced plasma irregularities over the Asian-  
250 Australian sector was larger in the main phase, but in the recovery phase, the American sector  
251 was larger. Therefore, five Ne profiles derived from Swarm-A during 24-28 August are plotted  
252 to describe the Asian-Australian ionospheric response during the main phase. These profiles  
253 not only have an adjacent longitude in  $\sim 120^\circ\text{E}$  to  $140^\circ\text{E}$  span, but also have a nearly observed  
254 time within UT05:10 to UT06:30, as shown the Ne tracks in Figure 4(a). Figure 4(b) shows the  
255 variation of daily Ne profiles as a function of geographic latitude, we can find that the plasma  
256 density kept in a low level with the peak density of  $\sim 5 \times 10^5 \text{el/cm}^3$  during 24-25 August. In the  
257 main phase, the topside Ne over the Asian-Australian sector significantly enhanced. The red  
258 curve expresses a significant structure of EIA on 26 August, the double plasma crests located  
259 at the  $10^\circ\text{N}$  to  $20^\circ\text{N}$  and  $0^\circ$  to  $10^\circ\text{S}$  latitudinal spans, respectively. Compared to the background  
260 values, the storm-enhanced Ne increased  $\sim 2$  times with a maximum value of  $\sim 1.05 \times 10^6 \text{el/cm}^3$ .  
261 The enhanced EIA is believed caused by a daytime “superfountain” effect that driven by the  
262 PPEFs. During strong geomagnetic storms, the PPEFs of eastward polarity could largely uplift  
263 the equatorial ionosphere over the sunlit and post-sunset sectors that drive the equatorial plasma  
264 along the geomagnetic field line to higher altitudes and expanded poleward latitudes with a  
265 significant enhancement of the EIA [Cherniak and Zakharenkova, 2022]. In the following two  
266 days, the intensity of EIA gradually decreased to a normal level.

267 Different from the sudden enhanced TECs over the Asian-Australian sector, the TEC’s  
268 change over the American sector in the main phase (25-26 August) was not significant.  
269 However, remarkable TEC enhancements were observed in the recovery phase, especially on  
270 28 August, the peak density occurred in the North America with a value of  $\sim 8 \times 10^5 \text{el/cm}^3$ . The  
271 hemispheric asymmetric structure of ionospheric TEC agrees well with the observations of  
272 ground-based radars and space-borne Swarm-A. Finally, the TEC’s changes over both the  
273 Asian-Australian and American sectors reveal that the magnetic storm not only enhanced the  
274 equatorial plasma density, but also triggered drastic polar ionospheric disturbances. The  
275 development of storm-induced polar ionospheric disturbances will be investigated in the  
276 following section.



277

278

279

280

281

282

283

284

285

286

287

288

289

290

291

**Figure 5.** Vertical sounder profiles of two chain ionosondes located at the Asian-Australian (left) and American sectors in a whole phase of geomagnetic storm, the dashed line signifies the onset of the main phase of the storm

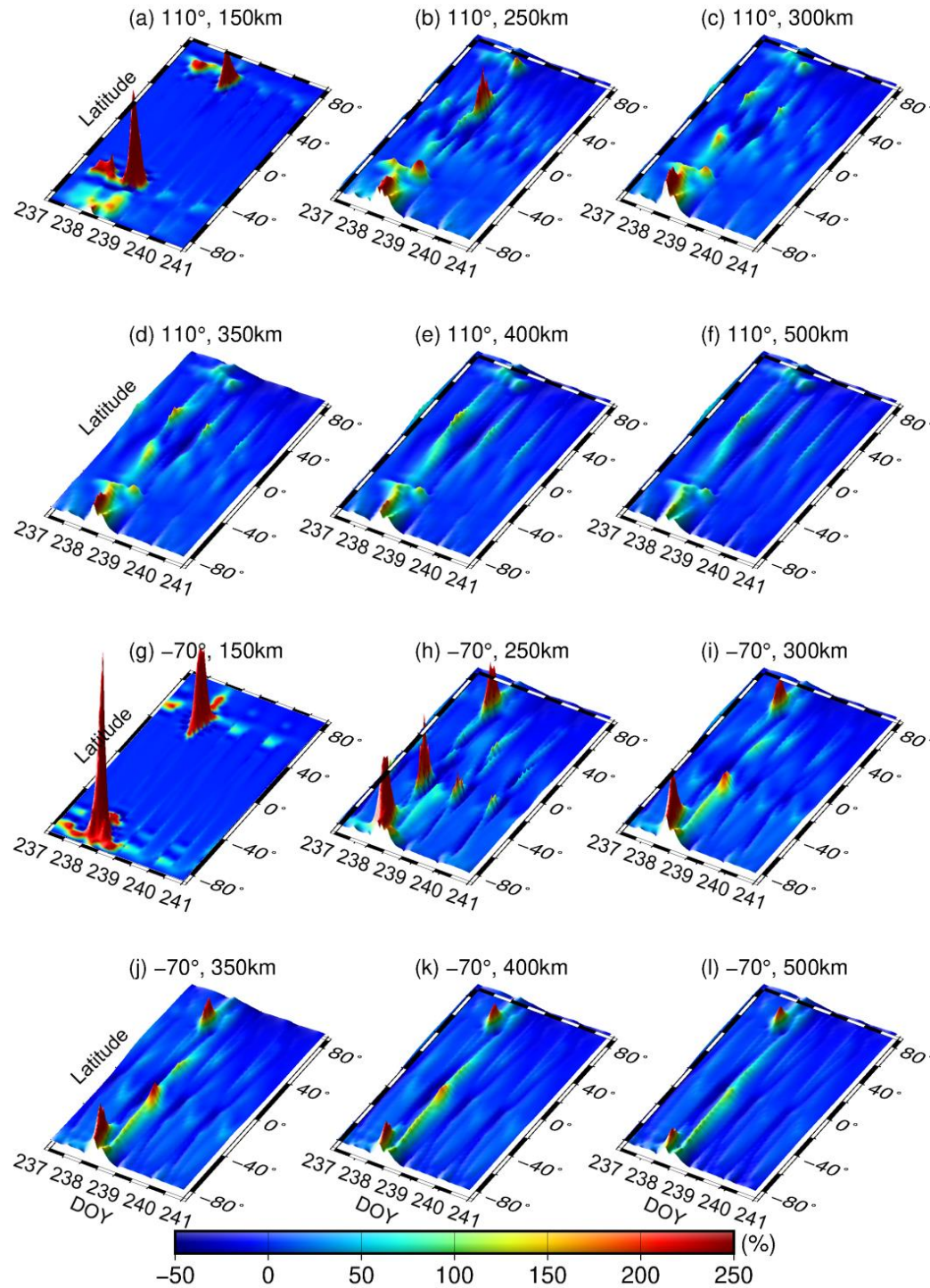
An ionosonde sounder is a radar that sweeps the high-frequency (HF) band signals and receives the echoes for examining the ionosphere and monitoring HF propagation conditions. Ionosonde primarily operates between 1.6MHz to 12 MHz. With this advantage, the two ionosonde chains located at the Asian-Australian and American sectors could detect the vertical dynamic propagation of storm-induced plasma irregularities, the results as shown in Figure 5. From the left panels, the radars located at the Asian-Australian sector detected HF signals with frequencies between 5.5 to 7MHz in the midnight-dawn (for local time, it was around the noon) during DOY235-240, and the HF signals accumulated under 200km. The equatorial radar detected HF plasma signal accumulated at a higher altitude. For example, Figure 5(c) shows the ionosonde GU513 located at the Guam measured a maximum frequency of 7MHz around the altitude of 250km in a minor solar-geomagnetic activity. After the onset of geomagnetic

292 storm, the plasma density during the midnight-dawn in the next day (26 August) suddenly  
293 enhanced and uplifted. As shown in the black arrows, enhanced HF plasma density were all  
294 detected over the equatorial and midlatitude radars (IC437, GU513, LM42B) in the main phase.  
295 Especially over the radar IC437, the peak height of ionosphere was uplifted above 350km with  
296 a peak frequency of 7MHz, and the intensity of Ne profiles in the northern hemisphere was  
297 significant stronger than that over dip-equator and southern hemisphere (GU513 and LM42B),  
298 which agreed well with the hemispheric asymmetric structure of plasma irregularities reported  
299 by [Astafyeva *et al.*, 2020].

300 The enhanced plasma was also detected by the radars located at the American sector. It  
301 should be noted that the blank areas over PQ052, GU513, MHJ45, WP937, JI91J signify the  
302 ionosondes failed to receive the HF echoes. It is found that the storm-enhanced plasma  
303 irregularities were observed in both of the main and recovery phase, Figure 5(h) had enough  
304 vertical profiles to describe the pattern. Also, this storm uplifted the peak height of ionosphere,  
305 but in the dawn-forenoon (it's around the midnight for local time). The largest intensity of  
306 plasma irregularities was detected over the dip-equatorial radar JI91J with a peak frequency of  
307 7MHz, and the ionospheric peak height was uplifted about 50-80km. Compared to the Asian-  
308 Australian sector, the hemispheric asymmetric structure was not significant. Finally, the  
309 detecting results of radars in low-middle latitudes manifested that the positive plasma  
310 irregularities primary accumulated between the altitudes of 200 to 300km. Finally, the radar  
311 PQ052 near the Arctic detected an interesting result, see the red arrow in Figure 5(a). During  
312 the recovery phase, significant positive plasma irregularities at the altitudes of 110 to 150km  
313 were observed near noon, DOY 239 (August 27). The different altitudinal behaviors of plasma  
314 irregularities indicated that significant positive plasma irregularities may be triggered only in  
315 the bottom-side of auroral ionosphere, rather than in the equatorial and mid-latitude ionosphere.

316 Due to the TEC maps and ionosondes fail to reveal the altitudinal structures of plasma  
317 irregularities, hence the plasma densities during DOY 235-240, 2018 are simulated by the TIE-  
318 GCM for solving this problem. The averaged plasma during DOY 235-236 are selected as  
319 background value, and the altitudinal changing percent of storm-induced plasma irregularities  
320 compared to background value is shown in Figure 6. Figure 6(a)-6(f) express the temporal  
321 variations of storm-induced plasma as a function of geographic latitude at the layers span from

322 150 to 500km along the meridian 110°, and the vertical scale is proportional to the changing  
 323 percent, which is represented by a color bar for better understand the storm-enhanced plasma  
 324 behaviors.



325

326 **Figure 6.** Ionospheric plasma disturbances at the layers span from 150 to 500km along the meridians 110°

327

(a-f) and -70° (g-l) during day of year (DOY) 237-240, 2018

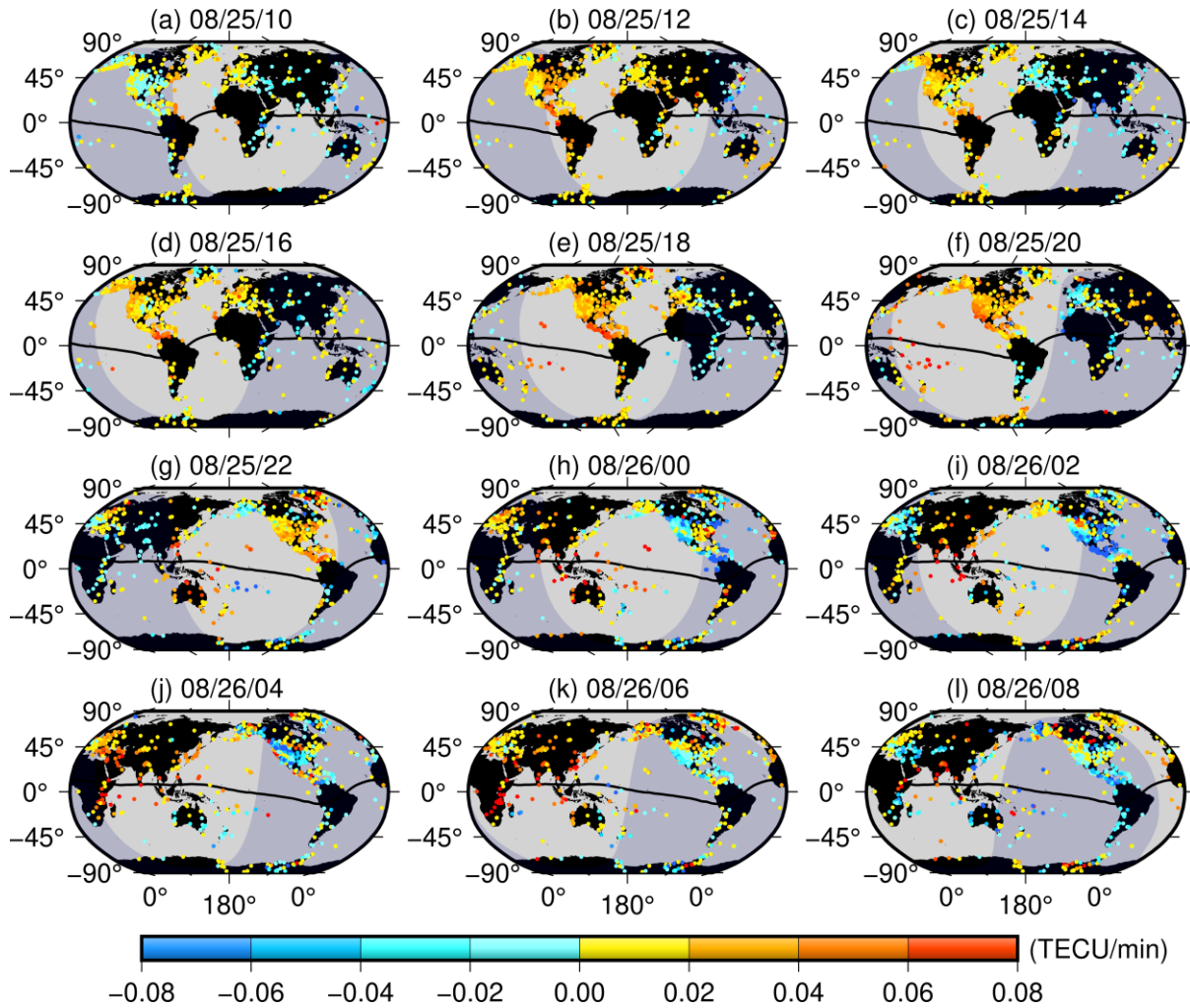
328 Figure 6 successes to simulate the development of double crests of the EIA at the altitudes  
329 of 150 to 500km. At the layer of 150km, since the main phase on DOY 237, two plasma  
330 increments appeared in 60°-65°N and 40°-45°S geographic latitudes along the meridian 110°,  
331 respectively. On the next day, the amplitude of plasma enhancements enhanced to 250%. At  
332 the same time, some tiny increments also occurred in the Antarctic. In the 250 km layer, the  
333 two plasma crests that located in 60°-65°N and 40°-45°S latitudes were weakened, while the  
334 plasma densities in the Antarctic were enhanced. With the increasing altitude, the plasma  
335 increments had an equatorward movement. For example, at the layer of 250 km, a plasma  
336 enhancement with a percent of ~200% appeared in 30°-40°N latitude, and a weaker increment  
337 located in 40°S latitude. The two low latitudinal enhancements moved equatorward within  $\pm 20^\circ$   
338 latitude at 350km layer. Above 350km, the two plasma crests merged into one unit and the EIA  
339 phenomena disappeared.

340 The change of ionospheric plasma along the meridian -70° agreed well with that over the  
341 Asian-Australian sector. Figure 6(g) shows two plasma increments appeared in 50°-60°N and  
342 60°-70°S latitude at 150km layer, and the maximum percent exceeded 250%. The EIA  
343 phenomenon was also observed within the layers of 250 to 350km, and the crests of the EIA  
344 enhanced about 200% in DOY 238. Compared to the Asian-Australian sector, the storm-  
345 induced plasma irregularities over the American sector were larger.

### 346 **3.3 Global ROTI in the main and recovery phase**

347 The results of Figure 3-5 reveal hemispheric asymmetric structures of plasma irregularities  
348 over two sectors in different phases. In order to further investigate the development of global  
349 storm-induced ionospheric irregularities, the Rate of total electron content Index change (ROTI)  
350 that expresses sharpness of the GNSS phase fluctuations caused by ionospheric irregularities  
351 and by strong spatial gradients of TEC is estimated by the ground-based receivers. Figure 7  
352 presents an overview of global GNSS ROTI maps during the main phase, and the time  
353 resolution of GNSS ROTI maps is one minute. The large positive and negative ROTI  
354 magnitudes are marked by red and blue, respectively; correspondingly, the small ROTI  
355 magnitudes are marked by yellow and cyan, respectively. At UT10, August 25, the ROTI map  
356 shows a low intensity of global ionospheric irregularities with an averaged value between -0.02

357 to 0.02TECU/min. From UT12, 25 August, the global ionospheric regularities abruptly  
 358 intensified. The positive plasma irregularities primary occurred in the sunlit sector, and the  
 359 magnitude of plasma irregularities over the Eastern Coast region of US and Mexico was largest  
 360 with a value of 0.06TECU/min. The plasma over the nighttime Greenland was also enhanced  
 361 about 0.02TECU/min.



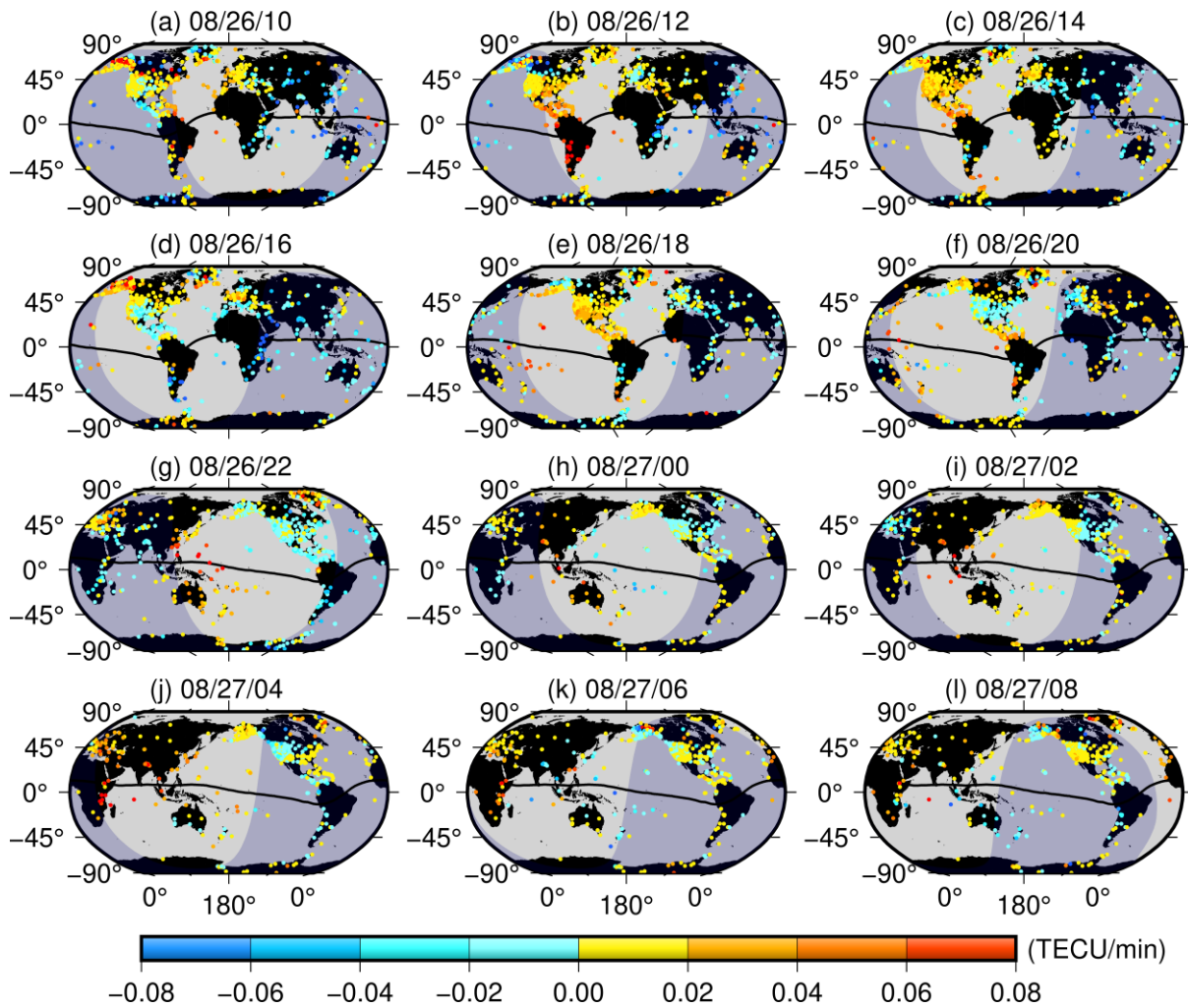
362  
 363 **Figure 7.** Global Navigation Satellite System Rate of total electron content (TEC) Index change (ROTI)  
 364 maps in the main phase (mm/dd/hh) of the geomagnetic storm. The black line signifies the magnetic  
 365 equator, and the shaded area shows nighttime.

366 After ~UT18, 25 August, the AE index rapidly increased above 500nT, even reached to a  
 367 peak of 1500 to 200nT in the main phase. Correspondingly, the daytime plasma irregularities  
 368 suddenly enhanced from UT18, 25 August, and significant hemispheric asymmetry of plasma  
 369 irregularities was observed in the American sector. Figure 7(e) shows the equatorial and auroral  
 370 plasma irregularities over the North America enhanced with a maximum magnitude of

371 0.08TECU/min, as well as the intensified mid-latitude plasma with a lower magnitude of  
372 0.06TECU/min. A narrow channel of positive ionospheric irregularities was registered along  
373 the western coast of North America in the northwestward direction, the latitudinal extent of  
374 EPBs reached to 20-25°N with a maximum value of 0.1TECU/min. In addition, the GNSS  
375 ROTI observations over some ground-based receivers located at several islands in the Pacific  
376 Ocean revealed an occurrence of positive storm-induced EPBs over 160°-140°W longitudinal  
377 span, the positive ionospheric irregularities were observed at both sides of the magnetic equator  
378 and their latitudinal extent was up to 25°- 27°N/S. The feature of equatorial ionospheric ROTI  
379 agreed well with the results reported by [Cherniak and Zakharenkova, 2022]. In the nighttime  
380 hemisphere, the ionospheric irregularities were negative with a low intensity. From 26 August,  
381 the GNSS ROTI over the Western Coast of The North America and Greenland turned negative,  
382 though some negative irregularities were under sunlit sector. However, the ROTI over the  
383 European-African sector gradually turned positive and enhanced to a largest magnitude during  
384 UT04-06, 26 August. The positive irregularities with a maximum value of 0.1TECU/min were  
385 observed in Europe, Africa and Asia, rather than Australia, though it was also under the sunlit  
386 sector. The results conclude that the hemispheric asymmetry of plasma irregularities was also  
387 significant during the ending of the main phase, which expresses the ROTI over Africa was  
388 larger than that over Europe, while it was opposite in the Asian-Australian sector.

389 Figure 8 shows an overview of global ionospheric irregularities during the recovery  
390 phase of the geomagnetic storm, it is found that the storm also induced strong GNSS ROTI,  
391 especially over the American sector. At UT10, 26 August, strong plasma irregularities with a  
392 level of 0.06TECU/min appeared over the South America, as well as the equator and mid-high  
393 latitudes of the North America. In addition, it is interesting that a narrow channel of positive  
394 ionospheric irregularities was observed in the northwestward direction over the nighttime  
395 Alaska. Two hours later, a significant hemispheric asymmetry of plasma irregularities  
396 developed over the American sector, which expresses the storm-induced plasma over 20°S to  
397 45°S latitudinal span enhanced larger than 0.08TECU/min, while the GNSS ROTI over the  
398 North America kept in a low level of 0.02 to 0.04TECU/min. Except the American sector, the  
399 plasma irregularities over other daytime or nighttime Continents maintained in a low level.  
400 From UT14, 26 August, the hemispheric asymmetry was reversed, which means high-

401 magnitude GNSS ROTI concentrated in the North America. Here, the signatures of the  
 402 ionospheric irregularities persisted for many hours till the midnight. Furthermore, significant  
 403 equatorial and mid-latitude positive plasma irregularities also appeared in the daytime Asian-  
 404 Australian and European-African sectors, as see Figure 8(g) and 8(j). In the following hours,  
 405 the global GNSS ROTI gradually recovered to a low level.



406

407

**Figure 8.** Similar to Figure 7, but in the recovery phase

408

### 3.4 Potential physical-chemical drivers of ionospheric irregularities

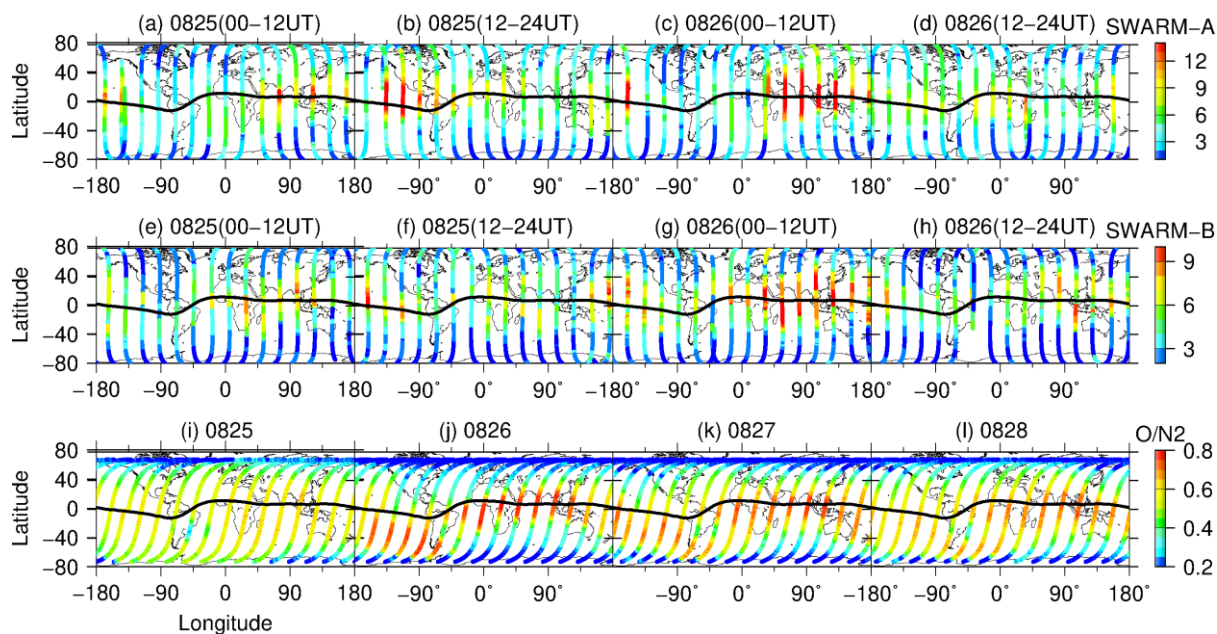
409

#### 3.4.1 Potential drivers of equatorial and mid-latitude ionospheric irregularities

410

Thermospheric composition change is an important driver in inducing positive or negative  
 411 ionospheric irregularities. Therefore, the thermospheric density ratio  $O/N_2$  measured by GUVI  
 412 on board the space-borne TIMED satellite (~625km) is analyzed. It is noted that the density  
 413 ratio  $O/N_2$  is a height integrated quantity within the orbit altitudes of the GNSS constellation

414 and the GUVI satellite. At the same time, the global topside TECs derived from Swarm-A and  
 415 Swarm-B are also investigated, and the TEC signifies the integrated electrons within the  
 416 altitudes from the orbit of Swarm microsatellite to the orbit of GNSS constellation. Figure 9  
 417 give an overview of daily topside TEC and  $O/N_2$  during the storm. One can also notice that the  
 418 TEC distribution is slightly different in the data of two satellites, which is most likely due to  
 419 the  $\sim 80\text{km}$  of difference in altitude. Both the profiles of Swarm-A and Swarm-B conclude that  
 420 the topside TECs over the Asian-Australian and American sectors were quiet before UT12, 25  
 421 August, the averaged TEC was under 6TECU. Figure 9(b) shows the TEC profile over the  
 422 American sector suddenly enhanced, and the expanded profiles covered the eastern Pacific,  
 423 this phenomenon was also validated by the observation of Swarm-B. During UT00-12, 26  
 424 August, the TEC over the Asia-Australia sector strengthened remarkably with a maximum  
 425 value of exceeded 12TECU. After that, the enhanced TEC profiles gradually decreased and  
 426 recovered to a normal level. The profiles derived from Swarm-B agreed well with that of  
 427 Swarm-A that large-scale positive TEC irregularities appeared over the Asian-Australian and  
 428 American sectors.



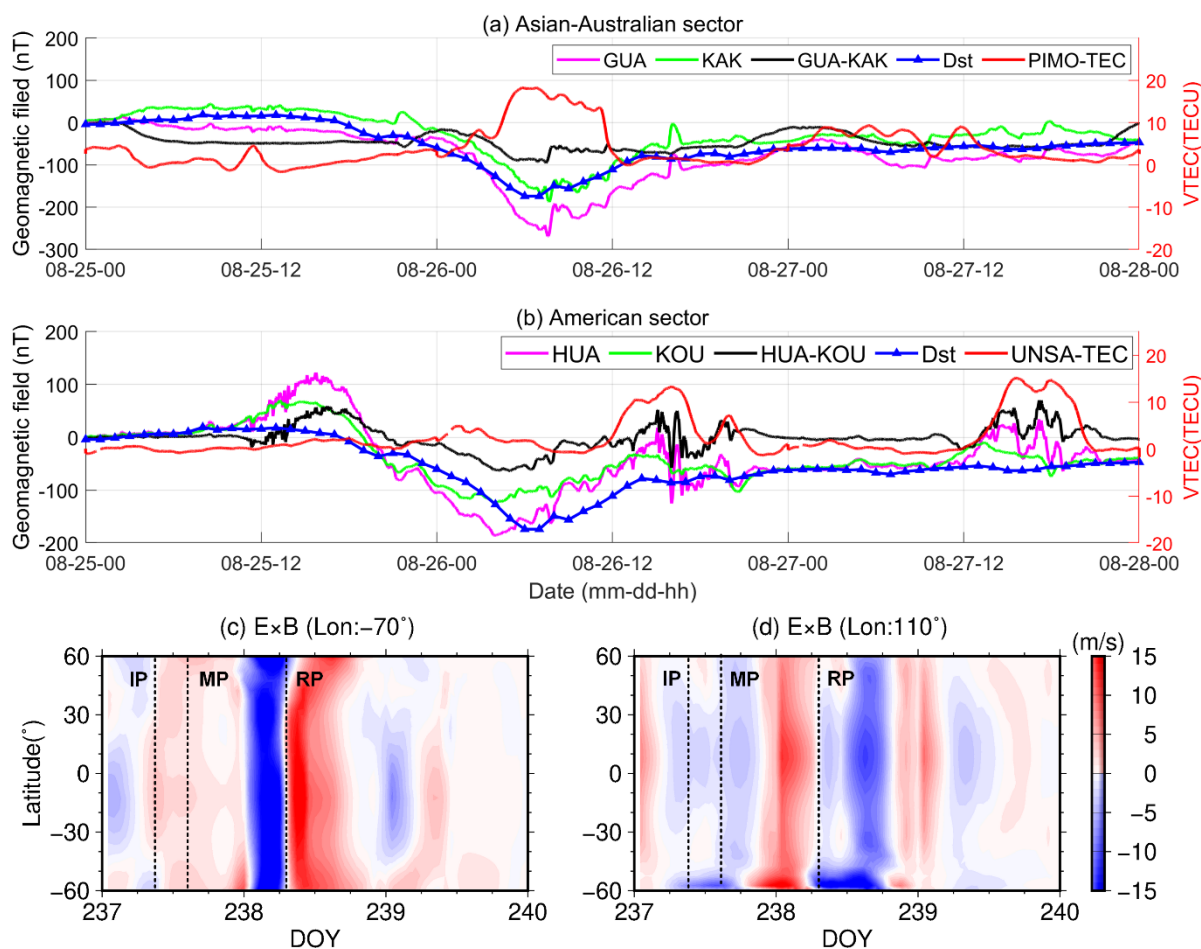
429  
 430 **Figure 9.** Topside TEC variations measured by GPS receivers on board the (a) – (d) Swarm-A and (e) – (h)  
 431 Swarm-B on 25-26 August, (i) – (l) thermospheric density ratio  $O/N_2$  as measured by the GUVI satellite  
 432 during August 25-28. The black thin curve signifies the magnetic dip equator.

433 Figure 9(i) shows the density ratio  $O/N_2$  was inversely proportional to geographic latitude,  
434 the  $O/N_2$  ranged from 0.3 to 0.6 in quiet days. However, the  $O/N_2$  ratio had a suddenly change  
435 with the eruption of a storm. Specifically, the  $O/N_2$  in low-middle latitudes increased  
436 remarkably with a maximum value of 0.8, while the  $O/N_2$  in Polar regions decreased to 0.2.  
437 Besides, the enhanced  $O/N_2$  had a southward excursion in the America sector. For example, see  
438 panel 9(j), the  $O/N_2$  in North America was about 0.4, while this ratio increased to 0.8 in South  
439 America. In the following two days, the storm-effect  $O/N_2$  gradually decreased with the  
440 geomagnetic field recovered to a normal level. The change of density ratio  $O/N_2$  agreed well  
441 with the TEC irregularities, which implied the change of density ratio  $O/N_2$  may be an  
442 important driver in generating plasma disturbances.  $O/N_2$  has a good positive correlation with  
443 plasma density, and it has proven to be a successful indicator of a neutral composition  
444 disturbance for analyzing ionospheric storms [Strickland *et al.*, 2001]. The ionospheric ion  
445 density loss rate is proportional to the molecular concentration, an increment of the mean  
446 molecular mass causes a decrement in electron density, while a decrement of molecular  
447 concentration provokes a positive disturbance.

448 As we know, at the altitudes of 90 to 130 km, many electrons move westward driven by  
449 dayside electric field. According to the equatorial dynamo effect, the westward electron flow  
450 generates a dayside eastward electric current, the electric current is defined as equatorial  
451 electrojet (EEJ). The EEJ could be severely suffered from the disturbed electric field  
452 penetrated from magnetosphere under a strong geomagnetic storm. The EEJ signatures can be  
453 estimated by taking the difference between the horizontal components performed by a pair of  
454 off-the-equator and at-the-equator magnetometers. The horizontal components of the  
455 magnetometers PHU, DLT, SJG and HUA located at the Asian-Australian and American sectors  
456 are used to investigate the storm-effect EEJ changes, and the observations of magnetometers  
457 are obtained from the International Real-time Magnetic Observatory Network  
458 (<https://intermagnet.org/index-eng.php>).

459 Figure 10(a) and 10(b) show the changes of EEJ signatures along with the Dst index over  
460 the Asian-Australian and American sectors. It is found that the Dst abruptly decreased with a  
461 geomagnetic storm erupted on UT14, 25 August 25 2018, as well as the horizontal components  
462 of the magnetometers PHU, DLT, SJG and HUA. In Figure 10(a), the equatorial magnetometer  
463 GUA decreased to a minimum value of  $\sim -270$ nT during UT 06-08, 26 August, and the

464 differential component between GUA and KAK had a negative perturbation with a minimum  
 465 value of -100nT. Correspondingly, the TEC over the station PIMO enhanced 18TECU in the  
 466 severest moment. The EEJ changes estimated by the difference between HUA and KOU in  
 467 Figure 10(b) agreed well with that over the Asian-Australian sector. The EEJ signature had two  
 468 distinct perturbations in the afternoons of 26-27 August with an amplitude of ~50nT. The  
 469 differential TEC over station UNSA was consistent with the EEJ signature. Two TEC  
 470 enhancements appeared in the recovery phase of geomagnetic storms, the maximum delta TEC  
 471 reached to 14TECU. The results demonstrate that the change of EEJ may be an important driver  
 472 in triggering storm-effect TEC disturbances. However, the slight EEJ fluctuations cannot fully  
 473 responsible for the strong TEC enhancements. Therefore, more drivers should be analyzed for  
 474 explaining the remarkable ionospheric disturbances.



475  
 476 **Figure 10.** Variations of the horizontal intensity of the geomagnetic field, equatorial electrojet (EEJ),  
 477 differential TECs and Dst value in the Asian-Australian (a) and American (b) sectors, as well as the  
 478 differential latitudinal vertical  $E \times B$  drifts along the  $-70^\circ$  (c) and  $110^\circ$  (d) longitudes.

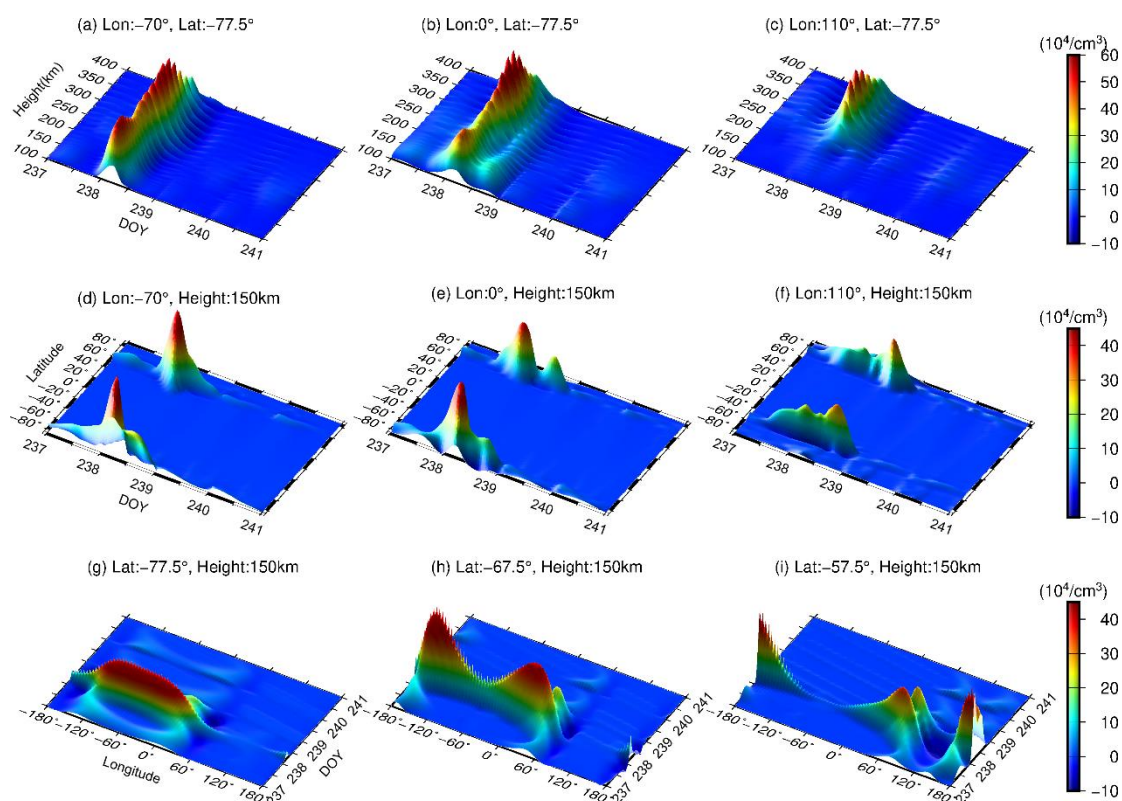
479 The equatorial plasma fountain effect plays a dominating role in generating the EIA. The  
480 vertical  $E \times B$  drift drives the equatorial plasmas upward to higher altitudes, and the accumulated  
481 plasmas diffuse down to higher latitudes along the geomagnetic field lines, which results two  
482 high concentrated plasma crests distributed on both sides of the magnetic equator [*Balan and*  
483 *Bailey, 1995; Li et al., 2021*]. In the fountain process, a stronger  $E \times B$  drift could lift more  
484 plasmas to higher altitudes, and the crests of EIA generated by the plasma diffused process are  
485 stronger and more poleward. Therefore, the changes of vertical  $E \times B$  drift may be another driver  
486 for the equatorial and mid-latitude plasma perturbations. The latitudinal changes of vertical  $E$   
487  $\times B$  drifts along the  $-70^\circ$  and  $110^\circ$  longitudes are simulated by the TIE-GCM in Figure 10(c)  
488 and 10(d). Figure 10(c) expresses the  $E \times B$  drifts along the meridian  $-70^\circ$  began to increase  
489 from UT14, 25 August, the slight  $E \times B$  enhancement was 3 to 5m/s. Then the nighttime  $E \times B$   
490 drifts suddenly weakened with a maximum decrement of -15m/s in the dawn, 26 August (LT,  
491 it was at night). Subsequently, the daytime differential  $E \times B$  drifts turned positive from UT8,  
492 26 August with a maximum increment of 15m/s. In the forenoon, 27 August (DOY 239), the  
493 differential  $E \times B$  had a hemispheric asymmetric structure, which expressed that the differential  
494  $E \times B$  on DOY 239 enhanced  $\sim 5$ m/s in the southern hemisphere. In the Asian-Australian sector,  
495 the  $E \times B$  drift enhanced from UT20, 25 August with a magnitude of 5 to 10m/s (LT, it was in  
496 daytime). In the following day, a slight positive  $E \times B$  irregularity was also observed.

497 The results in Figure 9-10 reveal that the thermospheric density ratio  $O/N_2$ , equatorial  
498 electrojet and vertical  $E \times B$  drift were suffered from the strong geomagnetic storm seriously.  
499 Among them, the equatorial electrojet was activated by the disturbed electric field penetrated  
500 from magnetosphere, and the changes of vertical  $E \times B$  drifts may be associated with PPEFs and  
501 DDEFs. Therefore, it is believed that the equatorial and mid-latitude ionospheric irregularities  
502 are a combined action of multiple physical-chemical processes. The enhanced density ratio  
503  $O/N_2$ , vertical  $E \times B$  drift and equatorial electrojet played a decisive role in inducing the positive  
504 irregularities. In the recovery phase, the hemispheric asymmetric  $O/N_2$  and  $E \times B$  drift on  
505 August 27 may be responsible for the asymmetric TEC over the American sector in Figure 3.

### 506 *3.4.2 Potential drivers of Auroral ionospheric irregularities*

507 The GNSS ROTI, sounder density profiles and TIE-GCM's simulations demonstrate  
508 significant Auroral ionospheric irregularities induced by the storm. For further to reveal the  
509 vertical structures of Auroral ionospheric irregularities, the plasma irregularities within the

510 altitude of 96 to 400km along the  $-70^\circ$ ,  $0^\circ$  and  $110^\circ$  longitudes are simulated by the TIE-GCM.  
 511 Figure 11(a) - 11(c) show the temporal variations of differential plasma density as a function  
 512 of altitude. In Figure 6, the TIE-GCM's simulation find that at the layer of 150km, largest  
 513 plasma irregularities with a changing percent of  $>250\%$  located in the  $70^\circ\text{S} - 80^\circ\text{S}$  latitude  
 514 span. Therefore, the geographic latitude is selected as  $77.5^\circ\text{S}$  in Figure 11(a) – 11(c). It should  
 515 be noted that the vertical scale of each panel is similar to Figure 7, but for the amplitude of  
 516 plasma irregularities. We can find that significant plasma enhancements occurred in topside  
 517 and bottom-side of the Antarctic ionosphere along three longitudes. In the main phase, the  
 518 increment along the meridian  $-70^\circ$  was maximum with a value up to  $6 \times 10^5 \text{el}/\text{cm}^3$ , followed by  
 519 the meridian  $0^\circ$ , the last was the weakest increment of  $4 \times 10^5 \text{el}/\text{cm}^3$  along the meridian  $110^\circ$ . In  
 520 addition, the plasma fluctuations were also observed in bottom-side ionosphere along the  
 521 meridians  $-70^\circ$  and  $0^\circ$ , except the meridian  $110^\circ$ .



522  
 523 **Figure 11.** Structures of differential plasma irregularities along the  $-70^\circ$ ,  $0^\circ$  and  $110^\circ$  longitudes as a  
 524 function of height (a-c), geographic latitude (d-f), and geographic longitude (g-i) during DOY 237 – 240.

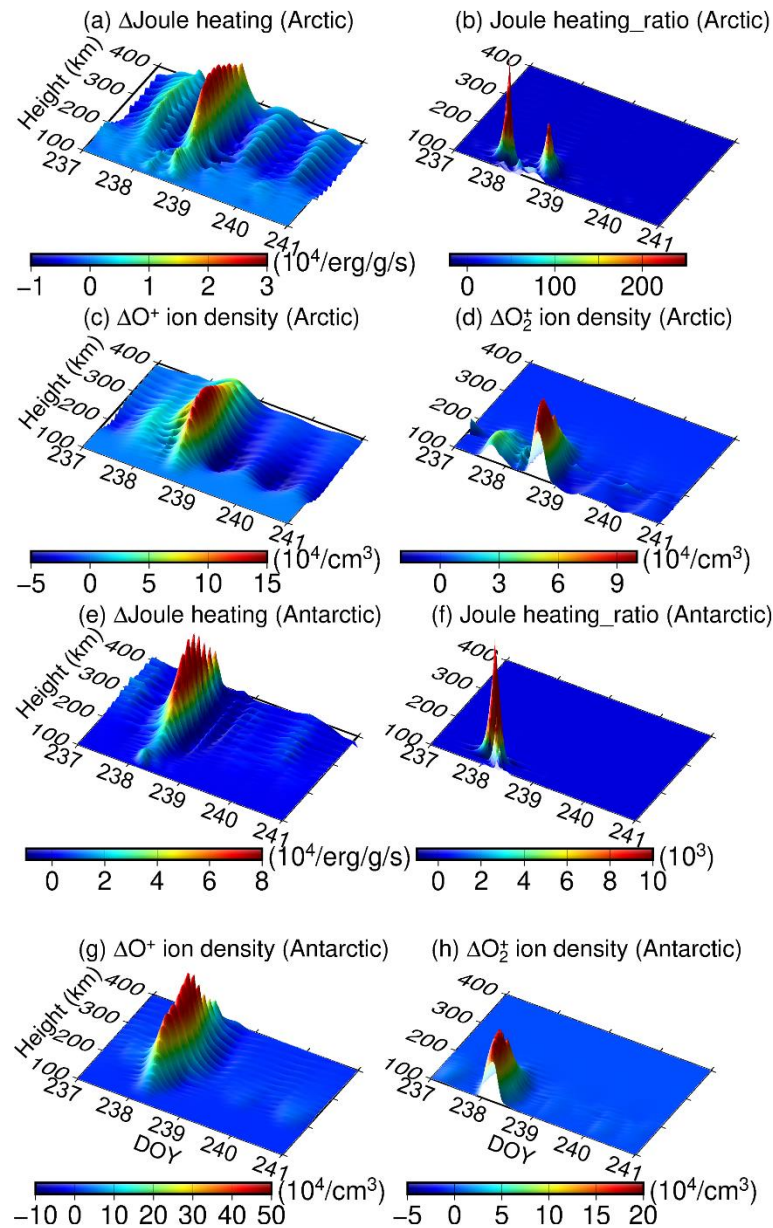
525 Did the geomagnetic storm only disturb the bottom-side ionosphere in the western  
 526 Antarctic? To address the question, the temporal variations of differential bottom-side plasma

527 (150km) as a function of geographic latitude along the meridians  $-70^\circ$ ,  $0^\circ$  and  $110^\circ$  are shown  
528 in panels 11(d) - 11(f). It is found that significant storm-effect plasma increments occurred in  
529 bottom-side ionosphere over all three longitudinal sectors, but the geographic latitudes of  
530 plasma increments were not stationary. Panel 11(d) shows two plasma crests were located in  
531  $60^\circ\text{N}$  and  $80^\circ\text{S}$  latitudes, respectively. The two crests had a northward movement in Eastern  
532 hemisphere. For example, in the Asian-Australian sector, the plasma crests moved to  $80^\circ\text{N}$  and  
533  $60^\circ\text{S}$  latitudes with a weaker value of  $3 \times 10^5 \text{el/cm}^3$ . The law of latitudinal motion of bottom-  
534 side plasma enhancements in different longitudinal sectors was associated with the asymmetric  
535 structure of geomagnetic field.

536 Figure 11(g) - 11(i) express the longitudinal structures of differential plasma (150km) as a  
537 function of day of year (DOY), the geographic latitudes in three sectors are  $77.5^\circ\text{S}$ ,  $67.5^\circ\text{S}$ ,  
538  $57.5^\circ\text{S}$ , respectively. Panel 11(g) reveals positive plasma irregularities occurred in  $-120^\circ \sim 0^\circ$   
539 longitudinal span on 26 August with a value of  $4 \times 10^5 \text{el/cm}^3$ . Along the  $67.5^\circ\text{S}$  latitude, the  
540 plasma irregularities had a double-peak structure that occurred in  $-180^\circ \sim 60^\circ$  longitudinal span.  
541 Along the  $57.5^\circ\text{S}$  latitude, the double-peak plasma increments were observed in  $0^\circ \sim 90^\circ$  and  
542  $150^\circ \sim -120^\circ$  longitudinal span. Compared to Auroral plasma irregularities, the intensity of  
543 bottom-side plasma irregularities decreased in middle geographic latitude. The results conclude  
544 that the strong storm not only induced topside plasma fluctuations, but also triggered positive  
545 bottom-side plasma irregularities near the Auroral zone ( $\sim > 50^\circ\text{N/S}$ ), which is consistent with  
546 the sounder profiles of the radar PQ052 in Figure 5(a).

547 In order to explain the development of Auroral ionospheric irregularities, the Joule heating,  
548  $\text{O}^+$  and  $\text{O}_2^+$  ion densities within the altitudes of 100 to 400 km are simulated by the TIE-GCM.  
549 In addition, the neutral mass density decreases exponentially with height, and the Joule heating  
550 per unit mass at higher altitude is much larger than that at the lower altitude. The bottom-side  
551 change will be neglected if only focus on the differential Joule heating per unit mass, thus the  
552 ratio of the changed Joule heating during storms compared to the quiet background values is  
553 also investigated. In the Arctic, the study area is selected at  $110^\circ\text{E}$ ,  $67.5^\circ\text{N}$ . The vertical changes  
554 of Joule heating, ratio of enhanced Joule heating,  $\text{O}^+$  and  $\text{O}_2^+$  ion density over the Arctic are  
555 shown in Figure 12(a) - 12(d). It is found that the Joule heating enhanced from the main phase  
556 with a magnitude of  $1 \times 10^4 \text{erg/g/s}$ , then the enhanced Joule heating reached a maximum in the

557 recovery phase with a value of  $3 \times 10^4$  erg/g/s. After that, the Joule heating gradually recovered  
 558 to backgrounds.



559  
 560 **Figure 12.** Vertical changes of Joule heating, ratio of enhanced Joule heating,  $O^+$  and  $O_2^+$  ion density over  
 561 the locations ( $110^\circ E$ ,  $67.5^\circ N$ , (a)-(d)) and ( $70^\circ W$ ,  $77.5^\circ S$ , (e)-(h)) during DOY237-240

562 Similar to the variation of topside Joule heating, the positive Joule heating disturbance was  
 563 also observed under 200km on DOY237-238 with a slight value of  $1 \times 10^4$  erg/g/s. Different  
 564 from the absolute change of the differential Joule heating in Figure 12(a), Figure 12(b) shows  
 565 the Joule heating in the main and recovery phases enhanced more 200 times than the  
 566 background values, and the maximum Joule heating enhancements were located in the altitudes

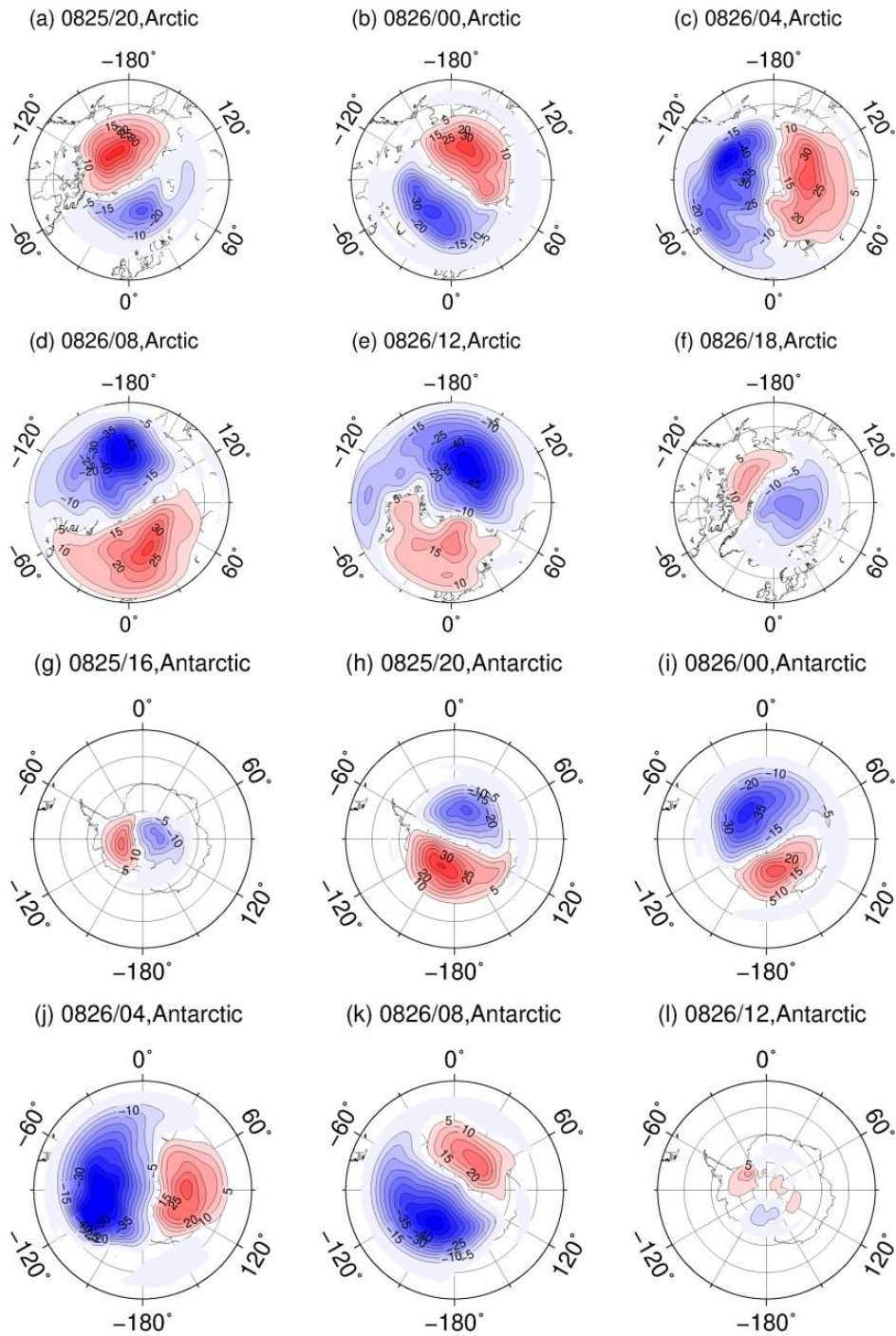
577 of 100-150km. The changes of O<sup>+</sup> ion density in panel 12(c) agreed well with the Joule heating,  
578 the O<sup>+</sup> ion density enhanced from DOY237 and grew stronger on DOY238 above the 200 km  
579 layer, the maximum value reached to  $1.5 \times 10^5/\text{cm}^3$ . An O<sub>2</sub><sup>+</sup> increment generated from UT14,  
570 DOY237, and grew to  $1 \times 10^5 \text{el}/\text{cm}^3$  on DOY238. Different from O<sup>+</sup> ion, the O<sub>2</sub><sup>+</sup> increments  
571 were mainly occurred under the 200 km layer, which is consistent with the behaviors of bottom-  
572 side enhanced Joule heating in Figure 12(b).

573 In the Antarctic, the study area is selected at 70°W, 77.5°S. The changes of Joule heating  
574 over the Antarctic agreed well that over the Arctic, but the positive Joule heating disturbances  
575 only appeared in the main phase, which is consistent with the variation of storm-effect Antarctic  
576 ionospheric plasma in Figure 11(a). The magnitude of enhanced Joule heating over the  
577 Antarctic was several times larger than that over the Arctic. Figure 12(e) expresses the topside  
578 and bottom-side Joule heating enhanced about  $8 \times 10^4 \text{erg}/\text{g}/\text{s}$  and  $2 \times 10^4 \text{erg}/\text{g}/\text{s}$ , respectively.  
579 However, Figure 12(f) indicates that the changed ratio of bottom-side Joule heating in the main  
580 phase was larger than that in the topside significantly, and the maximum enhanced ratio exceed  
581  $1 \times 10^4$ . Similar to Figure 12(c) - 12(d), in the main phase, the O<sup>+</sup> ion density over the Antarctic  
582 enhanced about  $5 \times 10^5/\text{cm}^3$  above the 200km layer, and the bottom-side O<sub>2</sub><sup>+</sup> ion density  
583 enhanced about  $2 \times 10^5 \text{el}/\text{cm}^3$ .

584 The changed amplitudes of Joule heating, O<sup>+</sup> and O<sub>2</sub><sup>+</sup> ion density over the Antarctic were  
585 much stronger than that over the Arctic, which agrees well with the magnitude of Polar  
586 ionospheric plasma disturbance in Figure 11. During a space weather event, the sudden  
587 enhanced energy could ionize the main neutral gases O<sub>2</sub> and N<sub>2</sub> that leads to an increment in  
588 ion density [*Gordon et al.*, 2020]. Our simulations confirmed the theory that the enhanced Joule  
589 heating could accelerate the Polar ionospheric ionization process, and the enhanced O<sup>+</sup> and O<sub>2</sub><sup>+</sup>  
590 ion densities are responsible for the topside and bottom-side plasma increments, respectively.

591 Geomagnetic storms not only form storm-enhanced densities (SEDs) in low-middle  
592 latitudes and tongues-of-ionization at the polar cap, but also change the global magnetic field  
593 and strength ionospheric-magnetospheric current systems [*Walach et al.*, 2021]. Ionosphere is  
594 a conductor, and the Polar ionosphere contains significant electric fields. The electric fields  
595 could drive the ionospheric current that close field-aligned currents flowing in the ionospheric-  
596 magnetospheric system, generate Joule heating in the upper atmosphere, and even control the

597 circulation of ionospheric plasma that change the Polar ionospheric electron density structure.  
 598 The ionospheric electric potential contour maps calculated with the Super Dual Auroral Radar  
 599 Network (SuperDRAN) Assimilative Mapping procedure ([http://vt.superdarn.org/tiki-](http://vt.superdarn.org/tiki-index.php?page=ASCIIData)  
 600 [index.php?page=ASCIIData](http://vt.superdarn.org/tiki-index.php?page=ASCIIData)) are used for investigating the spatial-temporal variations of the  
 601 Polar convection patterns in the main phase of the geomagnetic storm.



602

603 **Figure 13.** Maps of the electric potentials from SuperDARN over the Arctic (a-f) and Antarctic (g-l)  
 604 during August 25-26, 2018, the red and blue contours signify positive and negative potentials, respectively.

605 As shown in Figure 13, the positive and negative ionospheric electric potentials are  
606 indicated by red and blue contours. Usually the potential pattern has a maximum near dawn  
607 and a minimum near dusk. The difference between the maximum and minimum of potential is  
608 called the cross polar voltage. Figure 13(a) - f(f) gives an overview of the spatial-temporal  
609 evolution of electric potentials over the Arctic from UT20, 25 August to UT18, 26 August. At  
610 UT20, 25 August, a positive electric potential with a maximum value of 41kv distributed in -  
611  $90^{\circ} \sim -180^{\circ}$  longitudinal span, and the negative electric potential with a minimum magnitude  
612 of -32kv occurred in  $-60^{\circ} \sim 120^{\circ}$  longitudinal span. From 26 August, the Polar electric potential  
613 intensified remarkably with the decreasing Dst index. The strongest electric potential occurred  
614 in UT04-08, 26 August, concurrently with the AE index reached to a peak of 1500 to 2000nT.  
615 For example, the negative potential in Figure 13(d) dropped to -53kv, on the contrary, the  
616 positive potential enhanced to 36kv, and the cross polar voltage reached to 89kv. One can see  
617 that during the ending of the main phase, the convection zone in the Arctic extended  $\sim 50^{\circ}$ N,  
618 the scope of enhanced convection zone was consistent with the geographic latitude of radar  
619 PQ052 (Figure 2(a)) that was the station with a minimum latitude could detect the bottom-side  
620 ionospheric regularities. Similar to the Arctic electric potential, the scale and scope of electric  
621 potential over the Antarctica also enhanced and expanded remarkably. The negative potential  
622 dropped from -32kv at UT20, 25 August to -61kv at UT04, 26 August, while the corresponding  
623 positive potential reduced from 40kv to 33kv, the maximum cross polar voltage at the UT04,  
624 26 August reached to 94kv. The scale of Antarctic storm-effect electric potential was stronger  
625 than that over the Arctic, but the scope was smaller.

626 During active space weather events, the sudden energy and momentum deposited in the  
627 high-latitude ionosphere and thermosphere, mostly in the forms of particle precipitation and  
628 Joule heating. The incident precipitating particles gradually transfer energy to the different  
629 layers of the ionosphere, and ionize more charged particles as the stronger deposited energy.  
630 The accelerated ionization process enhances the ionospheric current flowing in the medium.  
631 The particle precipitation and Joule heating control the variations of the short-scale structures  
632 of the ionosphere-thermosphere, which results in an increment in the electric conductivity and  
633 heating of the ionosphere-thermosphere system. During the April 5, 2010 geomagnetic storm,  
634 the TIE-GCM simulations concluded that additional particle precipitation not only largely

635 increases ionospheric conductivity, but also causes remarkable Joule heating  
636 enhancements[Sheng *et al.*, 2017]. The enhanced conductivity, electric field, and a combination  
637 of both could intensify the ionospheric electric currents. The current density is proportional to  
638 the ionospheric conductivity directly, and the ionospheric conductivity is proportional to the  
639 plasma density directly [Cherniak and Zakharenkova, 2018]. Therefore, there is a close  
640 connection between magnetosphere energy deposition, particle precipitation, ionospheric  
641 currents intensification, Joule heating, and SEDs generation. Figure 12 - 13 reveal the plasma  
642 density, Joule heating and ionospheric electric potential affected by the storm all enhanced  
643 significantly, which further confirms the charged particles diffusion process reported by  
644 previous literatures. Thus, it is believed that the storm-induced Polar plasma irregularities are  
645 associated with the additional energy input through the ways of particle precipitation, Joule  
646 heating and ionospheric currents intensification.

#### 647 **4. Conclusion**

648 The 25-27 August geomagnetic storm was a surprising space event that generated in the  
649 background of very low solar activity. The prominent features of global ionospheric response  
650 to the strong geomagnetic storm that occurred at low solar activities are analyzed by ground-  
651 based instruments (GNSS receivers and ionosondes) and space-borne constellation (Swarm).  
652 This geomagnetic triggered several unusual ionospheric plasma irregularities depend on  
653 geographic longitude, latitude and altitude, and the potential drivers for explaining these  
654 irregularities are also discussed using the observations of magnetometers, GUVI profiles and  
655 TIE-GCM's simulations. Some important conclusions are drawn as follows:

656 (1) In the Asian-Australian sector, the observations of global GNSS receivers find that the  
657 storm enhanced the equatorial and mid-latitude TEC to a maximum value of 40TECU in the  
658 ending of main phase and the beginning of recovery phase. While in the American sector, this  
659 storm triggered a remarkable TEC hemispheric asymmetry in the recovery phase, which  
660 expresses TEC depletion occurred in North America, and low-level TEC enhancements  
661 occurred in mid-latitudes of South America. In the following two days, the equatorial and mid-  
662 latitude TEC over the American sector significant enhanced  $\sim 10$ TECU. The phenomenon was  
663 also validated by the ionospheric topside profiles derived from the Swarm-A, the space-borne

664 observations not only confirmed the plasma density enhancements over the Asian-Australian  
665 and American sectors that happened in the main and recovery phases, respectively, but also  
666 detected an enhanced double-peak crests of EIA that caused by a daytime “superfountain”  
667 effect that driven by the PPEFs.

668 (2) The sounder profiles of ionosondes found that the storm induced positive plasma  
669 irregularities in equatorial and mid-latitude ionosphere, and the enhanced plasma irregularities  
670 primary accumulated in altitudes of 200 to 300km with a maximum frequency of 7MHz.  
671 Different from TEC’s change, a hemispheric asymmetric structure of ionospheric vertical  
672 frequency was observed in the Asian-Australian sector, which expresses the topside (> 300km)  
673 plasma over the ionosonde IC437 located in northern hemisphere increased a maximum  
674 frequency of 7MHz. In addition, the profiles of the ionosonde PQ052 near the Arctic zone  
675 revealed an interesting finding, that is the storm could trigger positive plasma irregularities in  
676 the bottom-side (<150km) ionosphere near Auroral zone. Furthermore, the TIE-GCM  
677 succeeded to simulate the temporal variation of differential plasma density as a function of  
678 geographic latitude in the altitudes of 150 to 500km. The simulation not only discovered  
679 positive plasma irregularities with a ratio of > 250% at the layer of 150km, but also captured  
680 the development of the double crests of EIA in the altitudes of 250 to 400km.

681 (3) This study first time to give an overview of the development of global ROTI in the  
682 whole phase. The global ROTI maps found remarkable hemispheric asymmetry of plasma  
683 irregularities in a particular time. In the beginning of the main phase (UT12 – 22, 25 August),  
684 the ROTI in the American sector had a hemispheric asymmetric structure, which expressed the  
685 plasma irregularities in North America were larger than that in South America, the maximum  
686 irregularities appeared in Auroral zone and a narrow channel along the western coast of North  
687 America with a value of 0.1TECU/min. In the ending of the main phase, the plasma  
688 irregularities over Africa were larger than that in Europe, while it was opposite in the Asian-  
689 Australian sector. In the recovery phase, the GNSS receivers not only detected large plasma  
690 irregularities in nighttime Alaska, but also found a new hemispheric asymmetry in the  
691 American sector, which expressed the mid-latitude plasma with a positive ROTI of  
692 0.08TECU/min in South America was significantly larger than that in North America. The  
693 latitudinal plasma irregularities agreed well with TEC enhancements.

694 (4) The GUVI profiles indicated that the storm also induced significant thermospheric  
695 composition change during 26-27 August, which expressed positive density ratio  $O/N_2$  change  
696 occurred in equatorial ionosphere, and negative change appeared in Auroral zone. A  
697 hemispheric asymmetry of enhanced density ratio  $O/N_2$  was observed in South America. In  
698 addition, the EEJ were suffered from the enhanced equatorial electric field caused by  
699 geomagnetic storm slightly. The observations of magnetosphere demonstrated slight positive  
700 EEJ fluctuations occurred in the Asian-Australian and American sectors. Furthermore, the  
701 simulations of TIE-GCM concluded that the daytime  $E \times B$  drifts enhanced exceeded 15m/s in  
702 two sectors on 25-26 August. The enhanced  $E \times B$  drifts reinforced the equatorial fountain effect  
703 and strengthen the ionospheric double-peak structure at the layers of 250 to 350 km. The  
704 equatorial and mid-latitude plasma irregularities are believed to be a combined action of  
705 thermospheric composition change, equatorial electrojet, vertical  $E \times B$  drifts.

706 (5) The simulations of TIE-GCM demonstrated that the storm not only enhanced topside  
707 ionospheric plasma density, but also triggered positive plasma irregularities in bottom-side  
708 ionosphere near Auroral zone, which agreed well the observation of ionosonde PQ052. The  
709 bottom-side plasma irregularities had a poleward excursion along the magnetic equator, which  
710 was associated with the longitudinal offset of geomagnetic field. In addition, the positive Joule  
711 heating irregularities in the altitudes of 100 to 400km were observed in both Arctic and  
712 Antarctic, and the changed ratio of bottom-side Joule heating enhanced  $> 250\%$ . The temporal-  
713 spatial changes of Joule heating were consistent with the behaviors of Polar plasma  
714 irregularities. The enhanced  $O^+$  ion density was responsible for the topside plasma irregularities,  
715 and the increment of  $O_2^+$  ion density may be a dominating driver for the positive bottom-side  
716 plasma irregularities. Furthermore, the Polar ionospheric electric potential suffered from the  
717 storm severely, the cross polar voltage abruptly enhanced to 89kv and 94kv in the Arctic and  
718 Antarctic, respectively, and the enhanced electric potential expanded remarkably that the  
719 boundary reached to  $\sim 50^\circ N$  geographic latitude. The Polar ionospheric irregularities may be  
720 associated with the additional energy input through the ways of particle precipitation, Joule  
721 heating and ionospheric currents intensification.

722

723 **Acknowledgement:** The authors greatly appreciate the financial support from the Natural  
724 Science Foundation of Jiangsu Province (Grant Nos. BK20200646, BK20200664), and the  
725 Fundamental Research Funds for the Central Universities (Grant No. 2020QN31).

726 **Data Availability Statement:** The author acknowledge UNAVCO for GNSS observation files  
727 (<https://www.unavco.org/data/gps-gnss/gps-gnss.html>), Global Ionosphere Radio Observatory  
728 for sounder profiles (<jdbc:firebirdsql://didbase.giro.uml.edu/didb>), European Space Agency for  
729 SWARM profiles (<https://earth.esa.int/eogateway/missions/swarm/data>), GSFC for solar and  
730 geomagnetic indices (<https://omniweb.gsfc.nasa.gov/form/dx1.html>), INTERMAGNET for  
731 geomagnetic field data (<https://intermagnet.org/index-eng.php>), SuperDARN for ionospheric  
732 electric potential map (<http://vt.superdarn.org/tiki-index.php?page=ASCIIData>), High Altitude  
733 Observatory for the TIE-GCM model (<https://www.hao.ucar.edu/modeling/tgcm/tie.php>).

## 734 **Reference**

- 735 Aa, E., W. Huang, S. Liu, A. Ridley, S. Zou, L. Shi, Y. Chen, H. Shen, T. Yuan, and J. Li (2018),  
736 Midlatitude plasma bubbles over China and adjacent areas during a magnetic storm on 8  
737 September 2017, *Space Weather*, *16*(3), 321-331. <https://doi.org/10.1002/2017SW001776>
- 738 Astafyeva, E., I. Zakharenkova, and M. Förster (2015), Ionospheric response to the 2015 St.  
739 Patrick's Day storm: A global multi-instrumental overview, *Journal of Geophysical*  
740 *Research: Space Physics*, *120*(10), 9023-9037. <https://doi.org/10.1002/2015JA021629>
- 741 Astafyeva, E., M. S. Bagiya, M. Förster, and N. Nishitani (2020), Unprecedented hemispheric  
742 asymmetries during a surprise ionospheric storm: A game of drivers, *Journal of*  
743 *Geophysical Research: Space Physics*, *125*(3), e2019JA027261.  
744 <https://doi.org/10.1029/2019JA027261>
- 745 Atıcı, R., and S. Sağır (2020), Global investigation of the ionospheric irregularities during the  
746 severe geomagnetic storm on September 7–8, 2017, *Geodesy and Geodynamics*, *11*(3),  
747 211-221. <https://doi.org/10.1016/j.geog.2019.05.004>
- 748 Balan, N., and G. Bailey (1995), Equatorial plasma fountain and its effects: Possibility of an  
749 additional layer, *Journal of Geophysical Research: Space Physics*, *100*(A11), 21421-  
750 21432. <https://doi.org/10.1029/95JA01555>
- 751 Chang, H., H. Kil, A. K. Sun, S. R. Zhang, and J. Lee (2022), Ionospheric Disturbances in Low-

752 and Midlatitudes During the Geomagnetic Storm on 26 August 2018, *Journal of*  
753 *Geophysical Research: Space Physics*, 127(2), e2021JA029879.  
754 <https://doi.org/10.1029/2021JA029879>

755 Cherniak, I., and I. Zakharenkova (2018), Large-scale traveling ionospheric disturbances origin  
756 and propagation: Case study of the December 2015 geomagnetic storm, *Space Weather*,  
757 16(9), 1377-1395. <https://doi.org/10.1029/2018SW001869>

758 Cherniak, I., and I. Zakharenkova (2022), Development of the Storm-Induced Ionospheric  
759 Irregularities at Equatorial and Middle Latitudes During the 25-26 August 2018  
760 Geomagnetic Storm, *Space Weather*, 20(2), e2021SW002891.  
761 <https://doi.org/10.1029/2021SW002891>

762 Crowley, G., C. Hackert, R. Meier, D. Strickland, L. Paxton, X. Pi, A. Mannucci, A.  
763 Christensen, D. Morrison, and G. Bust (2006), Global thermosphere-ionosphere response  
764 to onset of 20 November 2003 magnetic storm, *Journal of Geophysical Research: Space*  
765 *Physics*, 111(A10). <https://doi.org/10.1029/2005JA011518>

766 de Paula, E. R., C. B. de Oliveira, R. G. Caton, P. M. Negreti, I. S. Batista, A. R. Martinon, A.  
767 C. Neto, M. A. Abdu, J. F. Monico, and J. Sousasantos (2019), Ionospheric irregularity  
768 behavior during the September 6–10, 2017 magnetic storm over Brazilian equatorial–low  
769 latitudes, *Earth, Planets and Space*, 71(1), 1-15. [https://doi.org/10.1186/s40623-019-](https://doi.org/10.1186/s40623-019-1020-z)  
770 1020-z

771 Dmitriev, A., A. Suvorova, M. Klimenko, V. Klimenko, K. Ratovsky, R. Rakhmatulin, and V.  
772 Parkhomov (2017), Predictable and unpredictable ionospheric disturbances during St.  
773 Patrick's Day magnetic storms of 2013 and 2015 and on 8–9 March 2008, *Journal of*  
774 *Geophysical Research: Space Physics*, 122(2), 2398-2423.  
775 <https://doi.org/10.1002/2016JA023260>

776 Durgonics, T., A. Komjathy, O. Verkhoglyadova, E. B. Shume, H.-H. Benzoni, A. J. Mannucci,  
777 M. D. Butala, P. Høeg, and R. B. Langley (2017), Multiinstrument observations of a  
778 geomagnetic storm and its effects on the Arctic ionosphere: A case study of the 19  
779 February 2014 storm, *Radio Science*, 52(1), 146-165.  
780 <https://doi.org/10.1002/2016RS006106>

781 Fuller-Rowell, T., M. Codrescu, R. Moffett, and S. Quegan (1994), Response of the

782 thermosphere and ionosphere to geomagnetic storms, *Journal of Geophysical Research:*  
783 *Space Physics*, 99(A3), 3893-3914. <https://doi.org/10.1029/93JA02015>

784 Gordon, E. M., A. Seppälä, and J. Tamminen (2020), Evidence for energetic particle  
785 precipitation and quasi-biennial oscillation modulations of the Antarctic NO<sub>2</sub> springtime  
786 stratospheric column from OMI observations, *Atmos. Chem. Phys.*, 20(11), 6259-6271.  
787 <https://doi.org/10.5194/acp-20-6259-2020>

788 Karatay, S. (2020), Temporal variations of the ionospheric disturbances due to the seasonal  
789 variability over Turkey using IONOLAB-FFT algorithm, *Geodesy and Geodynamics*,  
790 11(3), 182-191. <https://doi.org/10.1016/j.geog.2019.12.002>

791 Lei, J., F. Huang, X. Chen, J. Zhong, D. Ren, W. Wang, X. Yue, X. Luan, M. Jia, and X. Dou  
792 (2018), Was magnetic storm the only driver of the long-duration enhancements of daytime  
793 total electron content in the Asian-Australian sector between 7 and 12 September 2017?,  
794 *Journal of Geophysical Research: Space Physics*, 123(4), 3217-3232.  
795 <https://doi.org/10.1029/2017JA025166>

796 Li, W., J. Yue, Y. Yang, C. He, A. Hu, and K. Zhang (2018a), Ionospheric and thermospheric  
797 responses to the recent strong solar flares on 6 september 2017, *Journal of Geophysical*  
798 *Research: Space Physics*, 123(10), 8865-8883. <https://doi.org/10.1029/2018JA025700>

799 Li, W., D. Zhao, C. He, Y. Shen, A. Hu, and K. Zhang (2021), Application of a Multi-Layer  
800 Artificial Neural Network in a 3-D Global Electron Density Model Using the Long-Term  
801 Observations of COSMIC, Fengyun-3C, and Digisonde, *SPACE WEATHER*, 19(3),  
802 e2020SW002605. <https://doi.org/10.1029/2020SW002605>

803 Li, W., D. Zhao, C. He, C. M. Hancock, Y. Shen, and K. Zhang (2022), Spatial-temporal  
804 behaviors of large-scale ionospheric perturbations during severe geomagnetic storms on  
805 September 7-8 2017 using the GNSS, SWARM and TIE-GCM techniques, *Journal of*  
806 *Geophysical Research: Space Physics*, e2021JA029830.  
807 <https://doi.org/10.1029/2021JA029830>

808 Li, W., J. Yue, J. Guo, Y. Yang, B. Zou, Y. Shen, and K. Zhang (2018b), Statistical seismo-  
809 ionospheric precursors of M7. 0+ earthquakes in Circum-Pacific seismic belt by GPS TEC  
810 measurements, *Advances in Space Research*, 61(5), 1206-1219.  
811 <https://doi.org/10.1016/j.asr.2017.12.013>

812 Lissa, D., V. K. D. Srinivasu, D. Prasad, and K. Niranjana (2020), Ionospheric response to the  
813 26 August 2018 geomagnetic storm using GPS-TEC observations along 80 E and 120 E  
814 longitudes in the Asian sector, *Advances in Space Research*, 66(6), 1427-1440 %@ 0273-  
815 1177. <https://doi.org/10.1016/j.asr.2020.05.025>

816 Mannucci, A., B. Tsurutani, B. Iijima, A. Komjathy, A. Saito, W. Gonzalez, F. Guarnieri, J.  
817 Kozyra, and R. Skoug (2005), Dayside global ionospheric response to the major  
818 interplanetary events of October 29–30, 2003 “Halloween Storms”, *Geophysical Research*  
819 *Letters*, 32(12). <https://doi.org/10.1029/2004GL021467>

820 Mitchell, C. N., L. Alfonsi, G. De Franceschi, M. Lester, V. Romano, and A. Wernik (2005),  
821 GPS TEC and scintillation measurements from the polar ionosphere during the October  
822 2003 storm, *Geophysical Research Letters*, 32(12).  
823 <https://doi.org/10.1029/2004GL021644>

824 Nava, B., J. Rodríguez-Zuluaga, K. Alazo-Cuartas, A. Kashcheyev, Y. Migoya-Oru e, S. M.  
825 Radicella, C. Amory-Mazaudier, and R. Fleury (2016), Middle-and low-latitude  
826 ionosphere response to 2015 St. Patrick's Day geomagnetic storm, *Journal of Geophysical*  
827 *Research: Space Physics*, 121(4), 3421-3438. <https://doi.org/10.1002/2015JA022299>

828 Ngwira, C. M., J. B. Habarulema, E. Astafyeva, E. Yizengaw, O. F. Jonah, G. Crowley, A.  
829 Gisler, and V. Coffey (2019), Dynamic response of ionospheric plasma density to the  
830 geomagnetic storm of 22-23 June 2015, *Journal of Geophysical Research: Space Physics*,  
831 124(8), 7123-7139. <https://doi.org/10.1029/2018JA026172>

832 Qian, L., W. Wang, A. G. Burns, P. C. Chamberlin, A. Coster, S. R. Zhang, and S. C. Solomon  
833 (2019), Solar flare and geomagnetic storm effects on the thermosphere and ionosphere  
834 during 6–11 September 2017, *Journal of Geophysical Research: Space Physics*, 124(3),  
835 2298-2311. <https://doi.org/10.1029/2018JA026175>

836 Ramsingh, S. Sripathi, S. Sreekumar, S. Banola, K. Emperumal, P. Tiwari, and B. S. Kumar  
837 (2015), Low-latitude ionosphere response to super geomagnetic storm of 17/18 March  
838 2015: Results from a chain of ground-based observations over Indian sector, *Journal of*  
839 *Geophysical Research: Space Physics*, 120(12), 10,864-810,882.  
840 <https://doi.org/10.1002/2015JA021509>

841 Richmond, A., and G. Lu (2000), Upper-atmospheric effects of magnetic storms: a brief tutorial,

842 *Journal of Atmospheric and Solar-Terrestrial Physics*, 62(12), 1115-1127.  
843 [https://doi.org/10.1016/S1364-6826\(00\)00094-8](https://doi.org/10.1016/S1364-6826(00)00094-8)

844 Sheng, C., G. Lu, S. C. Solomon, W. Wang, E. Doornbos, L. A. Hunt, and M. G. Mlynczak  
845 (2017), Thermospheric recovery during the 5 April 2010 geomagnetic storm, *Journal of*  
846 *Geophysical Research: Space Physics*, 122(4), 4588-4599.  
847 <https://doi.org/10.1002/2016JA023520>

848 Shreedevi, P., R. Choudhary, S. V. Thampi, S. Yadav, T. Pant, Y. Yu, R. McGranaghan, E. G.  
849 Thomas, A. Bhardwaj, and A. Sinha (2020), Geomagnetic Storm-Induced Plasma Density  
850 Enhancements in the Southern Polar Ionospheric Region: A Comparative Study Using St.  
851 Patrick's Day Storms of 2013 and 2015, *Space Weather*, 18(8), e2019SW002383.  
852 <https://doi.org/10.1029/2019SW002383>

853 Spogli, L., D. Sabbagh, M. Regi, C. Cesaroni, L. Perrone, L. Alfonsi, D. Di Mauro, S. Lepidi,  
854 S. A. Campuzano, and D. Marchetti (2021), Ionospheric response over Brazil to the  
855 August 2018 geomagnetic storm as probed by CSES-01 and Swarm satellites and by local  
856 ground-based observations, *Journal of Geophysical Research: Space Physics*, 126(2),  
857 e2020JA028368. <https://doi.org/10.1029/2020JA028368>

858 Strickland, D. J., R. E. Daniell, and J. D. Craven (2001), Negative ionospheric storm coincident  
859 with DE 1-observed thermospheric disturbance on October 14, 1981, *Journal of*  
860 *Geophysical Research: Space Physics*, 106(A10), 21049-21062.  
861 <https://doi.org/10.1029/2000JA000209>

862 Walach, M. T., A. Grocott, and S. E. Milan (2021), Average Ionospheric Electric Field  
863 Morphologies during Geomagnetic Storm Phases, *Journal of Geophysical Research:*  
864 *Space Physics*, 126(4), e2020JA028512. <https://doi.org/10.1029/2020JA028512>

865 Zhang, R., L. Liu, H. Le, and Y. Chen (2019), Equatorial ionospheric electrodynamics over  
866 Jicamarca during the 6–11 September 2017 space weather event, *Journal of Geophysical*  
867 *Research: Space Physics*, 124(2), 1292-1306. <https://doi.org/10.1029/2020JA028512>

868